TU Delft

Delft University of Technology

Document Version
Final published version

Licence
Dutch Copyright Act (Article 25fa)

Citation (APA)
Liu, Q. F., Xiong, Q. X., Ji, L., Yang, J., Zhou, J., Meng, Z., Zhou, Y., & Tong, L. Y. (2026). Coupled modelling of hydration, calcium leaching, and sulfate attack in fly ash–blended cementitious materials. *Cement and Concrete Composites*, *171*, Article 106590. https://doi.org/10.1016/j.cemconcomp.2026.106590

Important note
To cite this publication, please use the final published version (if applicable).
Please check the document version above.

Copyright
In case the licence states “Dutch Copyright Act (Article 25fa)”, this publication was made available Green Open Access via the TU Delft Institutional Repository pursuant to Dutch Copyright Act (Article 25fa, the Taverne amendment). This provision does not affect copyright ownership.
Unless copyright is transferred by contract or statute, it remains with the copyright holder.

Sharing and reuse
Other than for strictly personal use, it is not permitted to download, forward or distribute the text or part of it, without the consent of the author(s) and/or copyright holder(s), unless the work is under an open content license such as Creative Commons.

Takedown policy
Please contact us and provide details if you believe this document breaches copyrights.
We will remove access to the work immediately and investigate your claim.

This work is downloaded from Delft University of Technology.

Cement and Concrete Composites 171 (2026) 106590



Contents lists available at ScienceDirect

Cement and Concrete Composites

journal homepage: www.elsevier.com/locate/cemconcomp



Coupled modelling of hydration, calcium leaching, and sulfate attack in fly ash–blended cementitious materials

Qing-feng Liu [a,b,c], Qing-xiang Xiong [b,c], Lie Ji [b,f], Jun Yang [a,d], Jianting Zhou [a,d], Zhaozheng Meng [b,e], Yu Zhou [b,g], Liang-yu Tong [b,*]

[a] State Key Laboratory of Mountain Bridge and Tunnel Engineering, Chongqing Jiaotong University, Chongqing, 400074, China
[b] State Key Laboratory of Ocean Engineering, Shanghai Jiao Tong University, Shanghai, China
[c] Shanghai Key Laboratory for Digital Maintenance of Buildings and Infrastructure, Shanghai, China
[d] School of Civil Engineering, Chongqing Jiaotong University, Chongqing, 400074, China
[e] Delft University of Technology, Stevinweg 1, 2628 CN, Delft, the Netherlands
[f] China State Construction Engineering Corporation Limited, Beijing, China
[g] Nanchang Water Authority, Nanchang, China

ARTICLE INFO

Keywords:
External sulfate attack
Low-calcium fly ash
Calcium leaching
Random porosity field
Numerical model

ABSTRACT

Low-calcium fly ash is widely used in cementitious materials to improve their resistance to external sulfate attack (ESA). This study presents a meso-scale numerical framework to evaluate the durability of systems incorporating different levels of fly ash under ESA conditions. The initial phase assemblage is determined using a hydration model that accounts for various fly ash chemical compositions and replacement ratios. The degradation process is simulated by coupling chemical reactions, ion transport, calcium leaching, porosity development, and mechanical damage. A random porosity field, characterized by both statistical distribution and spatial correlation, is introduced to represent material heterogeneity. Following model validation, the framework is applied to investigate the effects of sulfate concentration, specimen size, and fly ash content on sulfate resistance. The study further investigates the interaction between sulfate attack and calcium leaching, the influence of fly ash chemical composition on expansion strain, and the relationship between mineralogical indicators and ESA performance. Results indicate that neglecting the coupling between sulfate attack and calcium leaching leads to a significant underestimation of material degradation. In addition, smaller specimen sizes, neglecting porosity evolution, and a higher coefficient of variance (CV) of the porosity field result in increased expansion. Among the hydration products, the equivalent calcium aluminate (CA) content shows a positive linear correlation with expansion. Fly ash-related chemical indicators exhibit considerable variability and limited predictive accuracy; nevertheless, lower indicator values are generally associated with improved resistance to external sulfate attack.

1. Introduction

Cementitious materials has been recognized as one of the most economical and practical composite materials in the field of engineering [1] and has been used in various harsh environments, such as industrial and municipal wastewater, coastal area, salt lakes, and saline area [2–4]. However, in these sulfate-rich environment, cementitious structures will face crucial durability problems caused by external sulfate attack (ESA). The deterioration mechanism associated with ESA involves ion diffusion, chemical reactions, and expansion-induced damage [5,6]. Environmental sulfate ions penetrate into cementitious materials, leading to the formation of expansive products, the dissolution of portlandite (CH), and the decalcification of calcium silicate hydrates (C-S-H) [7,8]. Expansive compounds, such as gypsum and ettringite, exhibit low solubility and accumulate within the pore structure, resulting in microcrack formation, expansion of cement-based materials, and ultimately, structural failure or collapse [9,10]. As a result, developing effective and practical methods to assess and improve structural durability under aggressive environmental conditions has become a key focus in engineering research [11–13].

To enhance the durability performance of cementitious materials and reduce overall energy consumption, fly ash—a widely used supplementary cementitious material—has often been employed as a partial replacement for cement [31,32]. Previous experimental studies have

* Corresponding author.
E-mail addresses: liuqf@sjtu.edu.cn (Q.-f. Liu), tongly3@sjtu.edu.cn (L.-y. Tong).

https://doi.org/10.1016/j.cemconcomp.2026.106590
Received 4 August 2025; Received in revised form 6 March 2026; Accepted 19 March 2026
Available online 20 March 2026
0958-9465/© 2026 Elsevier Ltd. All rights are reserved, including those for text and data mining, AI training, and similar technologies.

generally shown that low-calcium fly ash can significantly improve the sulfate resistance of cementitious systems [23,25]. This improvement is primarily attributed to several synergistic mechanisms: the pozzolanic reaction consumes calcium hydroxide (CH), leading to a denser microstructure and refined pore network; the dilution effect reduces the content of tricalcium aluminate (C_3A), which is responsible for forming expansive ettringite in the presence of sulfates; and the overall reduction in permeability slows down the ingress of sulfate ions [26,21]. In contrast, high-calcium fly ash may reduce sulfate resistance, particularly when used in high dosages. This reduction is often linked to the higher content of reactive calcium compounds, such as free lime (CaO) and CH, which can increase the availability of reactants for sulfate attack [24]. Therefore, the phase assemblage of fly ash–blended cementitious materials after hydration plays a key role in sulfate resistance. To better evaluate the sulfate resistance of blended materials, the interactions between the pozzolanic reaction and cement hydration should be thoroughly considered, taking into account various factors such as the water-to-binder ratio, fly ash type, and replacement level.

Moreover, to scrutinize the deterioration mechanism and sulfate resistance performance of cementitious materials under ESA, scholars designed different models to study its long-term durability [33–35]. Sarkar et al. [36] simulated the degradation process under ESA considering the ion diffusion, chemical reaction and mechanical damage accumulation. Yu et al. [37] modelled ion transport during ESA with the considering of diffusion, electrical coupling, chemical activity, advection and cracking suction. Zhang et al. [38] proposed a transport-chemical-physical-mechanical model for concrete subjected to ESA and drying-wetting cycles. Qin et al. [39] used numerical model evaluating the effect of calcium leaching and temperature variations on ESA mechanisms of cementitious materials. However, most existing models have been developed for ordinary Portland cement (OPC) systems [40–43], and suitable numerical models for evaluating the sulfate resistance of fly ash–blended cementitious materials remain limited. A pioneering effort was made by Nie et al. [44], who developed a numerical model that incorporated the pozzolanic reaction to analyze and simulate the influence of fly ash on sulfate attack. However, this model did not account for the interaction between calcium leaching and sulfate ingress, nor did it consider porosity changes resulting from concurrent dissolution and precipitation processes. In reality, calcium leaching happens if the cementitious materials was subjected to a poorly mineralized or acid solution [45]. The calcium leaching process has been reported to be closely associated with sulfate attack, begins with the dissolution of CH and is followed by the decalcification of C-S-H [46,47]. Not only the leached calcium ions will affect the chemical reaction rates, the looser pore structure due to leaching process will also affect the ion transport and ultimate the sulfate attack [41,48]. Expect for the effect of calcium leaching on sulfate attack, many experiments have also verified that the sulfate solution will affect calcium leaching greatly. For example, Zou et al. [49] discovered a leaching acceleration phenomenon in a sulfate solution. Phung et al. [50] further found that the degree of acceleration is highly related to the concentration of the acid solution. B. Gerard et al. [51] proposed a solid-liquid equilibrium curve to depict the whole leaching process. Benefitting from its convenience, this leaching model was widely accepted in many scholars' research [52,53]. Wan et al. [54] corrected the leaching curve for concrete in a 6 mol/L acid solution with reference to the principle of charge conservation. Zou et al. [49] draw a similar conclusion that the calcium leaching behavior of cementitious materials in the sulfate solution follows the typical three-stage curve. Therefore, to fully understand the behavior and underlying mechanisms of fly ash–blended cementitious materials under ESA, a comprehensive numerical model should be developed that accounts for the interaction between sulfate attack and calcium leaching, with particular attention to the often-overlooked accelerating effect of sulfates on calcium dissolution.

Additionally, as typical porous materials, pore structure of cementitious materials serves as both transport channels and reaction cites for the diffusion-reaction deterioration process, and play an important influential factor [55–57]. Ran et al. [58] used a mercury porosimeter to monitor the pore size distribution. The findings showed that expansive compounds fill the big pores at first without volume expansion, and subsequently induce microcracks between the mortar. Chen et al. [59] found that the sulfate-induced damage mainly owes to the nucleation and growth of delayed ettringite, and the initial pore size which is dependent on water-to-cement ratio can influence the damage evolution significantly. Currently, the changeable pore structure during ESA and its reverse effect on ESA have also attracted many scholars' attention, and been considered in some numerical studies. For example, Tixier et al. [60] proposed a chemical sulfate attack model based on the diffusion-reaction approach, which considered the volume increase of crystals in the system to simulate the ESA. Yin et al. [61] conducted a comprehensive review of the ESA models in recent years and emphasized the importance of incorporating the volume change of concrete pore and accounting for the damage effect resulting from chemical reactions. However, existing models often simplify cementitious materials as isotropic and homogeneous, assuming a uniform initial porosity throughout the domain; in reality, however, these materials contain randomly distributed porosities [62]. The consideration of microstructural features significantly influences the modelling accuracy [63]. For example, Bao et al. [20] found the predicted carbonation depths of cementitious materials with a non-uniform porosity field are more irregular and are much closer to the experimental values. Tong et al. demonstrated that incorporating pore distribution enhances the prediction accuracy of both carbonation [64] and chloride penetration depths [65,66]. In the field of ultrasonic detection of void content in composite materials, Lin et al. [67] developed a two-dimensional porosity model based on the ellipsoidal autocorrelation function, which accounts for spatial correlations. It is evident that an uneven porosity distribution will influence the ion transport properties, subsequently impacting chemical reactions, cracking profiles, and the overall degradation process of ESA. Given the small pore size in cementitious materials, accurately capturing pore distribution at the meso- or macro-scale in numerical models remains challenging. Employing a random distribution field to characterize both the porosity magnitude and spatial inhomogeneity of cementitious materials would be a more effective approach.

To fill the abovementioned research gap, this study proposes a meso-scale model to evaluate the degradation mechanism of fly ash-blended cementitious materials under ESA, incorporating the interaction between sulfate attack and calcium leaching. The hydration process is first analyzed to determine the initial phase assemblage prior to ESA. A random porosity field—accounting for both probability density distribution and spatial correlation—is employed to represent the heterogeneous porosity distribution. The chemical reactions, ionic transport, calcium leaching, porosity evolution, and mechanical damage are comprehensively integrated to model degradation process. Model validation is conducted using third-party experimental data, covering both hydration and degradation stages. Furthermore, to investigate the influence of intrinsic material properties on deterioration, a parametric study is carried out, focusing on the contents of calcium aluminate, calcium silicate, and calcium hydroxide. The proposed model is hoped to better understand the underlying mechanisms and provide an effective approach to predict the degradation process for cementitious materials exposed to the sulfate-rich environments.

2. Numerical modelling of sulfate attack from hydration to degradation

To numerically investigate the sulfate resistance of fly ash-blended cementitious materials under ESA, Section 2.1 introduces a hydration model for blended systems that accounts for the chemical compositions of fly ash and cement, mixture proportions, and pozzolanic reactions. Next, Section 2.2 describes a random porosity field based on a specified

probability density function and an ellipsoidal autocorrelation function to represent the heterogeneous initial porosity filed. Finally, Section 2.3 presents a comprehensive chemo-transport-damage model for ESA degradation process, incorporating chemical reactions, ionic transport, calcium leaching, porosity evolution, and crack development.

2.1. Hydration model for the cement blended with low-calcium fly ash

Due to the incorporation of fly ash, the cementitious matrix becomes a binary system involving both cement hydration and pozzolanic reactions. As a result, the fractions of hydrated and unreacted products in such a binary cement–fly ash system cannot be accurately predicted using conventional cement hydration models. To address this limitation, the present study proposes a modified Papadakis model to calculate the mass fractions of hydration and pozzolanic reaction products, accounting for the cement hydration degree and the pozzolanic activity of fly ash [16]. Given that existing experimental studies have demonstrated the superior sulfate resistance of low-calcium fly ash, this study focuses primarily on systems incorporating low-calcium fly ash. In the model, both Portland cement and fly ash are analyzed in terms of their oxide compositions, namely: CaO (C), SO_3 ($\bar{S}$), Al_2O_3 (A), Fe_2O_3 (F), SiO_2 (S), bound water (H). The mass fractions of the constituent i ($i = C, \bar{S}, A, F,$ and S) in the cement and fly ash is defined as w_i^c and w_i^{FA}, respectively. During hydration, the chemical reaction of the mineral component of Portland cement can be expressed as:

$$2C_3S + 6H \rightarrow C_3S_2H_3 + 3CH \tag{1}$$

$$2C_2S + 4H \rightarrow C_3S_2H_3 + CH \tag{2}$$

$$C_3A + C\bar{S}H_2 + 10H \rightarrow C_4A\bar{S}H_{12} \tag{3}$$

$$C_4AF + 2CH + 10H \rightarrow C_6AFH_{12} \tag{4}$$

The presence of calcium hydroxide (CH) could initiate the pozzolanic reaction with the reactive fly ash. The simplified pozzolanic activity of the low-calcium fly ash can be described as:

$$2S + 3CH \rightarrow C_3S_2H_3 \tag{5}$$

$$A + C\bar{S}H_2 + 3CH + 7H \rightarrow C_4A\bar{S}H_{12} \tag{6}$$

$$A + 4CH + 9H \rightarrow C_4AH_{13} \tag{7}$$

As proposed by Papadakis [16], two different cases can be distinguished according to the level of total gypsum ($C\bar{S}H_2$) present. If the gypsum content is higher than that theoretically required for full hydration of the cement and complete pozzolanic reaction of fly ash alumina, as:

$$m_{C\bar{S}H_2} > \left(1.689w_A^c - 1.078w_F^c\right)m_c + 1.689\gamma_A \cdot w_A^{FA} \cdot m_{FA} \tag{8}$$

It should be noted that Papadakis's model assumes complete hydration of cement and full pozzolanic activity of fly ash, which are rarely achieved in practice [68]. Therefore, this study further refines the Papadakis model by incorporating the reaction rates of both cement and fly ash. Then, the mass of CH, $C_3S_2H_3$ (CSH), $C_4A\bar{S}H_{12}$ ($CA\bar{S}H$), C_6AFH_{12} (CAFH), C_4AH_{13} (CAH), remaining constituents (R) and bound water (H) can be written as following, in kg/m^3:

$$\begin{aligned} m_{CH} = &\left\{1.321\left(w_C^c - 0.7w_{\bar{S}}^c\right) - \left(1.851w_S^c + 2.182w_A^c + 1.392w_F^c\right)\right\} \cdot \alpha_c \cdot m_c \\ &-\left(1.851\gamma_S \cdot w_S^{FA} + 2.182\gamma_A \cdot w_A^{FA}\right) \cdot \alpha_{FA} \cdot m_{FA} \end{aligned} \tag{9}$$

$$m_{CSH} = 2.85\left(w_S^c \cdot \alpha_c \cdot m_c + \gamma_S \cdot w_S^{FA} \cdot \alpha_{FA} \cdot m_{FA}\right) \tag{10}$$

$$m_{CA\bar{S}H} = \left(6.106w_A^c - 3.898w_F^c\right) \cdot \alpha_c \cdot m_c + 6.106\gamma_A \cdot w_A^{FA} \cdot \alpha_{FA} \cdot m_{FA} \tag{11}$$

$$m_{CAH} = 0 \tag{12}$$

$$m_{CAFH} = 5.099w_F^c \cdot \alpha_c \cdot m_c \tag{13}$$

$$\begin{aligned} m_H = &\left\{0.321\left(w_C^c - 0.7w_{\bar{S}}^c\right) + 1.236w_A^c \right. \\ &\left. -0.113w_F^c\right\} \cdot \alpha_c \cdot m_c + 1.236\gamma_A \cdot w_A^{FA} \cdot \alpha_{FA} \cdot m_{FA} \end{aligned} \tag{14}$$

$$m_R = (m_c + m_{FA} + m_w) - (m_{CH} + m_{CSH} + m_{CA\bar{S}H} + m_{CAH} + m_{CAFH} + m_H) \tag{15}$$

the corresponding porosity of the specimen can be predicted as:

$$\begin{aligned} \varnothing = &\frac{m_w}{1000} - \left\{0.249\left(w_C^c - 0.7w_{\bar{S}}^c\right) + 0.191w_S^c \right. \\ &\left. + 1.118w_A^c - 0.357w_F^c\right\} \cdot \alpha_c \cdot \frac{m_c}{1000} - \left(1.18\gamma_A \cdot w_A^{FA}\right) \cdot \alpha_{FA} \cdot \frac{m_{FA}}{1000} \end{aligned} \tag{16}$$

where m_c, m_{FA} and m_w represent the mass of cement, fly ash and water before hydration, γ_i is the weight fraction of the oxide i in the pozzolan that contributes to the pozzolanic reactions ("active" ratio). α_c and α_{FA} are the hydration degree of cement and fly ash, respectively.

On the contrary, if the gypsum content is lower than that required for cement hydration and for complete pozzolanic reaction of the active part of fly ash alumina. Then it is assumed that **Eq. (6)** takes place until all gypsum is consumed, and the remaining active A reacts only with CH according to the reaction in **Eq. (7)** giving C_4AH_{13} (CAH). In this case, the mass contents of different phases are calculated as:

$$\begin{aligned} m_{CH} = &\left(1.321w_C^c - 1.851w_S^c - 2.907w_A^c - 0.928w_F^c\right) \cdot \alpha_c \cdot m_c \\ &-\left(1.851\gamma_S \cdot w_S^{FA} + 2.907\gamma_A \cdot w_A^{FA}\right) \cdot \alpha_{FA} \cdot m_{FA} \end{aligned} \tag{17}$$

$$m_{CSH} = 2.85\left(w_S^c \cdot \alpha_c \cdot m_c + \gamma_S \cdot w_S^{FA} \cdot \alpha_{FA} \cdot m_{FA}\right) \tag{18}$$

$$m_{CA\bar{S}H} = 7.774w_{\bar{S}}^c \cdot \alpha_c \cdot m_c \tag{19}$$

$$m_{CAH} = \left(5.497w_A^c - 3.509w_F^c - 7w_{\bar{S}}^c\right) \cdot \alpha_c \cdot m_c + 5.497\gamma_A \cdot w_A^{FA} \cdot \alpha_{FA} \cdot m_{FA} \tag{20}$$

$$m_{CAFH} = 5.099w_F^c \cdot \alpha_c \cdot m_c \tag{21}$$

$$\begin{aligned} m_H = &\left(0.321w_C^c - 0.675w_{\bar{S}}^c + 1.590w_A^c - 0.339w_F^c\right) \cdot \alpha_c \cdot m_c \\ &+1.590\gamma_A \cdot w_A^{FA} \cdot \alpha_{FA} \cdot m_{FA} \end{aligned} \tag{22}$$

$$m_R = (m_c + m_{FA} + m_w) - (m_{CH} + m_{CSH} + m_{CA\bar{S}H} + m_{CAH} + m_{CAFH} + m_H) \tag{23}$$

the corresponding porosity of the specimen can be predicted as:

$$\begin{aligned} \varnothing_0 = &\frac{m_w}{1000} - \left\{0.249\left(w_C^c - 0.1w_{\bar{S}}^c\right) + 0.191w_S^c \right. \\ &\left. + 1.059w_A^c - 0.319w_F^c\right\} \cdot \alpha_c \cdot \frac{m_c}{1000} - \left(1.121\gamma_A \cdot w_A^{FA}\right) \cdot \alpha_{FA} \cdot \frac{m_{FA}}{1000} \end{aligned} \tag{24}$$

In the present study, the Avrami model is used to describe the hydration degree of cement, as [69]:

$$\alpha_c(t) = 1 - \exp\left(-k_c \cdot t^{n_c}\right) \tag{25}$$

where k_c is the rate constant dependent on water to cement ratio (w/c), as $k_c = 0.02 \cdot \exp(2 - 5w/c)$; n_c is the reaction order, estimated from C_3S content, as $n_c = 1.5 + 0.5w_{C_3S}^c$ [70]. Fly ash reactivity is modelled with a delayed exponential function due to a certain time is required before the pozzolanic reaction can be activated [71]:

$$\alpha_{FA}(t) = \alpha_{FA,max}\left[1 - \exp\left(-k_{FA} \cdot (t - t_d)^{n_{FA}}\right)\right] \cdot H(t - t_d) \tag{26}$$

where $\alpha_{FA,max}$ is the maximum attainable hydration degree of fly ash, determined as the mass fraction of active phase $\alpha_{FA,max} = \gamma_S \cdot w_S^{FA} + \gamma_A \cdot w_A^{FA}$; k_{FA} is the rate constant for fly ash reaction, related to CaO

content in fly ash, as $k_{FA} = 0.03 + 0.05w_C^{FA}$; n_{FA} is the reaction order; t_d is the delayed time before fly ash reaction starts, 3 days is assumed in this study; $H(t - t_d)$ is the Heaviside function [71–73]. The model validation will be carried out in Section 3.1.

2.2. Random field model of porosity

Cementitious materials are typical porous materials consist of randomly distributed porosities in cement mortar at different place. While the average porosity can be considered a large-scale uniform property, local deviations from this average represent small-scale non-uniformities [67]. To capture this uneven characteristic in the numerical model, this study adopts a random porosity field that accounts for both probability density distribution and spatial correlation, following the methodologies of Yu et al. [74] and Bao et al. [20], in which similar random field formulations were successfully applied to carbonation studies of cementitious materials. Although the underlying degradation mechanisms differ, the statistical description of pore structure heterogeneity remains applicable. Accordingly, the distribution type and correlation structure are kept consistent with these studies. The porosity field of cement mortar is therefore assumed to follow a lognormal distribution, as expressed in Eq. (27).

$$P(\varnothing) = \frac{1}{\delta\varnothing\sqrt{2\pi}}\exp\left[-\frac{(\ln(\varnothing)-\mu)^2}{2\delta^2}\right] \tag{27}$$

where $\varnothing$ is the random porosity field taking between 0 and 1, $P(\varnothing)$ is the probability density of $\varnothing$; μ and δ are the log mean and log standard deviation. The relationship between μ, δ, the average porosity $\varnothing_a$ and the variance of porosity ν can be expressed by **Eqs. (28)** and **(29)**. The coefficient of variance (CV) is calculated by **Eq. (30)**:

$$\mu = \ln\left(\frac{\varnothing_a^2}{\sqrt{\nu+\varnothing_a^2}}\right) \tag{28}$$

$$\delta = \sqrt{\ln\left(\frac{\nu}{\varnothing_a^2}+1\right)} \tag{29}$$

$$CV = \frac{\sqrt{\nu}}{\varnothing_a} \tag{30}$$

Further to describe the spatial correlation effect of randomly distributed porosity, an ellipsoidal function is used as [67]:

$$f(x,y) = \exp\left[-\left(\frac{x^2}{a^2}+\frac{y^2}{b^2}\right)^{\frac{1}{1+r}}\right] \tag{31}$$

where f is an ellipsoidal autocorrelation function; a and b are the autocorrelation length in the x and y directions, respectively, and are assumed to be 0.005 m in the present study. r is the roughness factor; in this study, $r = 0$ is adopted, corresponding to a Gaussian autocorrelation function.

As illustrated in Eqs. (27-30), the average porosity and CV are the key parameters governing the randomly distributed characteristics of the porosity field. In this study, reference is made to the Jiang's work [75], in which porosity values at different locations within cementitious samples were experimentally measured. Their results indicate that the spatial variability of local porosity is relatively limited, with a CV of approximately 0.1. Moreover, the ratio between the maximum and minimum local porosity values was reported to be on the order of 2–3, a range that is also consistent with observations in other studies (e.g., Ref. [76]). Based on these experimental findings, a CV of 0.1 is adopted in the present study.

Using the method that incorporates both the Fourier transform and inverse Fourier transform as described in Yu et al. [74], the spatial distribution of random porosity, considering the aforementioned autocorrelation function, can be generated. A representative random porosity field, accounting for spatial correlation effects, is depicted in Fig. 1(a). The average porosity is set at 15%, with a coefficient of variation (CV) of 0.1. The probability density corresponding to Fig. 1(a) is presented in Fig. 1(b) and compared with the target probability given by Eq. (27) as well as the experimental data reported in Ref. [75]. The results indicate that the generated porosity values range between 0 and 1. Furthermore, the comparison demonstrates a good agreement between the generated and target log normal distributions. In contrast to a uniform porosity assumption, the random porosity field accounts for spatial heterogeneity in the pore structure. This heterogeneity affects local diffusion pathways, the accumulation of reactive species, and the development of expansion-induced stresses. A quantitative comparison with the uniform porosity case is provided in the following sections.

2.3. Chemo-transport-damage model for sulfate attack

Fig. 2 illustrates the schematic diagram for the proposed meso-scale chemo-transport-damage model for sulfate attack, which integrates the coupled processes of ESA and calcium leaching. These processes begin with ion transport and leaching, which alter the chemical composition of the pore solution, disrupting local equilibrium and triggering chemical reactions (Section 2.3.1). Calcium leaching is described using a solid–liquid equilibrium curve, with the accelerating effect of sulfate ions also taken into account (Section 2.3.2). As precipitation and dissolution occur during the process, the pore structure evolves over time, leading to changes in the transport properties of cementitious materials (Section

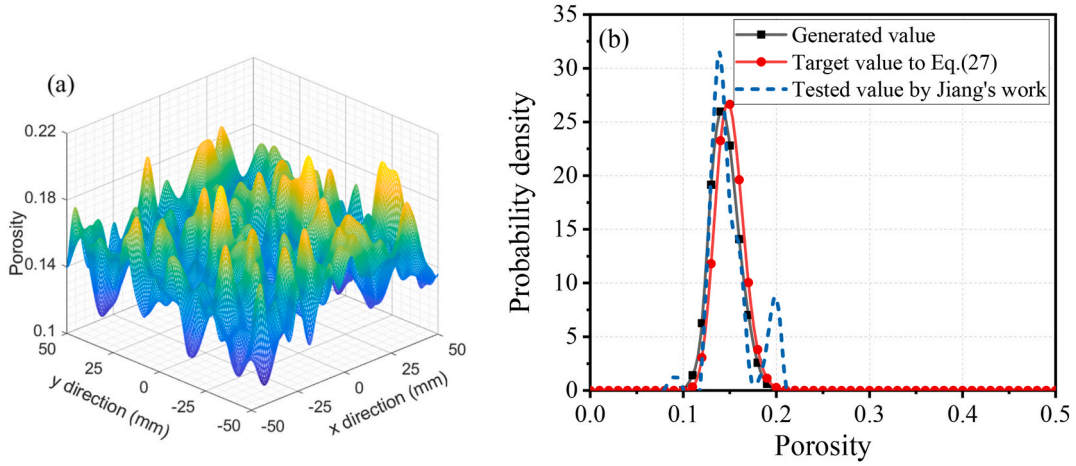


Fig. 1. Example of random porosity field (a) Generated spatial porosity distribution (b) Validation of generated probability density.

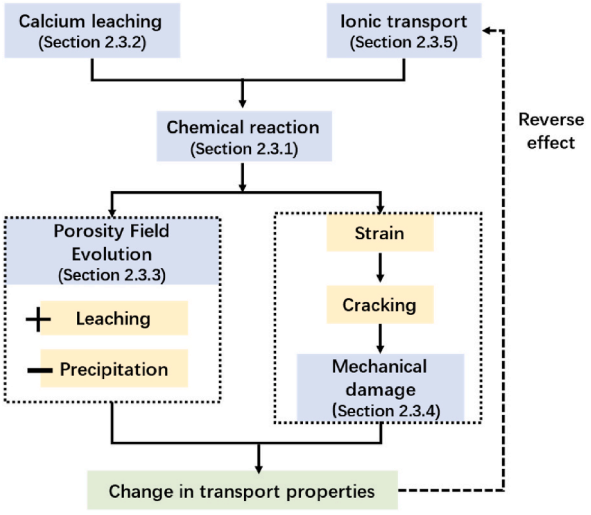


Fig. 2. Schematic diagram for the proposed chemo-transport-damage model.

2.3.3). Meanwhile, volume changes in solid phases induce strain and microcracks, which are represented by a damage parameter (Section 2.3.4). These changes in porosity and cracking, in turn, modify diffusivity, further influencing ionic transport (Section 2.3.5). The following sections provide a detailed description of the specific methodologies used in each part of the model.

2.3.1. Chemical reactions

When external sulfate ions penetrate cementitious materials, a series of chemical reactions occur, ultimately leading to material deterioration [77]. In this study, sodium sulfate solution is selected as the sulfate source, and the influence of different cation types on the chemical reactions is not considered. Consequently, the formation of gypsum ($C\bar{S}H_2$) is initiated through the reaction between sulfate ions and dissolved calcium ions released from calcium hydroxide (CH) and calcium silicate hydrates (C-S-H):

$$Ca^{2+} + SO_4^{2-} + 2H \rightarrow C\bar{S}H_2 \tag{32}$$

The gypsum ($C\bar{S}H_2$) further reacts with both hydrated and unreacted calcium aluminates to form ettringite ($C_6A\bar{S}_3H_{32}$), as described by Eqs. (33-35). To reduce computational costs in the rigorous chemo-transport-damage model, a detailed chemical thermodynamic analysis of the solid-liquid solubility equilibrium is not considered. Instead, a meso-scale approach incorporating simplified mass balance and time-dependent reaction kinetics is adopted. Additionally, it should be noted that due to the low reaction rate between tetracalcium aluminoferrite (C_4AF) and gypsum, the corresponding reaction is not concluded [78]. In the proposed model, three different calcium aluminate phases—tricalcium aluminate (C_3A), tetracalcium aluminate (C_4AH_{13}), and monosulfate ($C_4A\bar{S}H_{12}$)—are taken into account.

$$C_3A + 3C\bar{S}H_2 + 26H \rightarrow C_6A\bar{S}_3H_{32} \tag{33}$$

$$C_4AH_{13} + 3C\bar{S}H_2 + 14H \rightarrow C_6A\bar{S}_3H_{32} + CH \tag{34}$$

$$C_4A\bar{S}H_{12} + 2C\bar{S}H_2 + 16H \rightarrow C_6A\bar{S}_3H_{32} \tag{35}$$

Based on the previous research done by Tixier [8], the chemical reaction between gypsum and calcium aluminate phases can be integrated in the lumped form as:

$$CA + qC\bar{S}H_2 \rightarrow C_6A\bar{S}H_{32} \tag{36}$$

where CA is an equivalent grouping of reacted calcium aluminate phases, with $CA = \lambda_1 C_3A + \lambda_2 C_4AH_{13} + \lambda_3 C_4A\bar{S}H_{12}$; λ_i represents the molar fraction of the reacted calcium aluminate phases and can be calculated as $\lambda_i = m_i / \sum_{i=1}^{3} m_i$; m_i is the molar concentration of calcium aluminate phases (mol/^{3}), which can be calculated through the hydration model; q is the stoichiometric coefficients of lumped reaction and can be calculated as $q = 3\lambda_1 + 3\lambda_2 + 2\lambda_3$. In the present study, hydration and sulfate attack are treated separately rather than fully coupled. The hydration model is used to determine the initial phase assemblage, while coupled sulfate attack and calcium leaching processes are considered during the subsequent degradation analysis. Fully coupled hydration-degradation modeling will be explored in future work. It is important to note that the primary objective of Eq. (36) is to determine the stoichiometric coefficients of the main reactants and products involved in external sulfate attack. As a result, certain substances, such as water and calcium hydroxide, are not explicitly included in the simplified representation, and the equation is therefore not fully balanced.

According to the reaction kinetic laws, Eq. (32) and (36) could be assumed as second-order equations. Therefore, the reaction rate of sulfate ions and calcium ions consumption (due to gypsum formation during ESA), as well as calcium aluminates consumption and gypsum precipitation caused by ESA can be obtained as [39,22]:

$$\frac{\partial C_{SO_4^{2-}}}{\partial t} = -k_1 C_{SO_4^{2-}} C_{Ca^{2+}} \tag{37}$$

$$\left(\frac{\partial C_{Ca^{2+}}}{\partial t}\right)_{ESA} = -k_1 C_{SO_4^{2-}} C_{Ca^{2+}} \tag{38}$$

$$\frac{\partial C_{gpy}}{\partial t} = k_1 C_{SO_4^{2-}} C_{Ca^{2+}} - k_2 C_{CA} C_{gpy} \tag{39}$$

$$\frac{\partial C_{CA}}{\partial t} = -k_2 \frac{C_{CA} C_{gpy}}{q} \tag{40}$$

where $C_{SO_4^{2-}}$ and $C_{Ca^{2+}}$ are the molar concentration of sulfate and calcium ions in pore solution, respectively (mol/m^3); C_{CA} and C_{gpy} are the solid content of equilibrium grouping of reacted calcium aluminate phases and gypsum, respectively (mol/m^3), where the consumption of one unit of gypsum corresponds to the consumption of calcium aluminate with a stoichiometric factor of $1/q$; k_1 (3.05×10^{-8} m^3/mol/s) and k_2 (1.22×10^{-9} m^3/mol/s) are the traction rate constant of Eq. (32) and (36), according to Ref. [79].

2.3.2. Calcium leaching

During sulfate penetration, calcium ions that participate in reactions with sulfate ions primarily originate from the dissolution of calcium hydroxide (CH) and the decalcification of calcium silicate hydrate (C-S-H) gel. The process of calcium leaching leads to an increase in porosity, subsequently reducing the material's mechanical strength and further accelerating ESA [36,80,81]. Moreover, the concentration of calcium ions in the pore solution plays a crucial role in governing reaction kinetics. Therefore, incorporating the calcium leaching process into the chemo-transport-damage model enhances the reliability of ESA simulations. Given the inherent uncertainties in the chemical equilibrium mechanisms of C-S-H, the calcium leaching effect is typically represented using a solid–liquid equilibrium curve, which can be expressed as [53]:

$$C^S_{Ca^{2+}} = \begin{cases} C_{CSH0}\left(\dfrac{C_{Ca^{2+}}}{C_{satu}}\right)^{1/3}\left(-\dfrac{2}{x_1^3}C_{Ca^{2+}}^3 + \dfrac{3}{x_1^2}C_{Ca^{2+}}^2\right) & 0 \le C_{Ca^{2+}} \le x_1 \\ C_{CSH0}\left(\dfrac{C_{Ca^{2+}}}{C_{satu}}\right)^{1/3} & x_1 < C_{Ca^{2+}} \le x_2 \\ C_{CSH0}\left(\dfrac{C_{Ca^{2+}}}{C_{satu}}\right)^{1/3} + \dfrac{C_{CH0}}{(C_{satu}-x_2)^3}(C_{Ca^{2+}}-x_2)^3 & x_2 < C_{Ca^{2+}} \le C_{satu} \end{cases} \tag{41}$$

where $C^{S}_{Ca^{2+}}$ is the calcium ion concentration in solid phase (mol/m^3); C_{satu} is the calcium ion concentration in the saturated liquid phase (mol/m^3); C_{CSH0} and C_{CH0} represent the initial molar concentration of CH and C-S-H (mol/m^3); x_1 is the calcium ion concentration in pore solution signifying the decalcification of C-S-H gel (mol/m^3); x_2 is the calcium ion concentration in pore solution signifying the dissolution of CH (mol/m^3).

As illustrated in the schematic representation of calcium leaching in Fig. 3, Eq. (41) consists of three distinct stages. For ordinary Portland cement exposed to pure water, the parameters x_1 and x_2 are typically set to 2 mol/m^3 and 17 mol/m^3 respectively [53]. However, several studies have demonstrated that when cementitious materials are exposed to aggressive solutions, such as sodium chloride or ammonium nitrate, the calcium leaching process is significantly accelerated [50,54,82]. Therefore, the influence of sulfate ions in accelerating calcium leaching should also be taken into account. Based on experimental investigations conducted by Zou et al. [49], x_1, x_2 and C_{satu} should be correlated with sulfate concentration as follows:

$$x_1 = 0.388\sqrt{C_{s0}} + 1.309 \tag{42}$$

$$x_2 = 0.897 C_{satu} \tag{43}$$

$$C_{satu} = \begin{cases} 0.1754 C_{s0} + 22.68 & C_{s0} < 315.5\text{mol/m}^3 \\ 78.1 & C_{s0} > 315.5\text{mol/m}^3 \end{cases} \tag{44}$$

where C_{s0} is the concentration of the sulfate solution. Therefore, the reaction rate of calcium ions induced by leaching effect can be determined as:

$$\left(\frac{\partial C_{Ca^{2+}}}{\partial t}\right)_{Leach} = -\frac{\partial C^{S}_{Ca^{2+}}}{\partial t} \tag{45}$$

It is worth noting that, to date, experimental and analytical studies specifically addressing the calcium leaching equilibrium behavior of fly ash-blended cementitious materials under sulfate attack remain limited; therefore, this study adopts the model proposed by Zou et al. [49] as a basis for calcium leaching modelling.

2.3.3. *Effect of porosity evolution on transport properties*

Sulfate attack induces the formation of gypsum and ettringite, leading to the expansion of cementitious materials [83]. While the expansion mechanisms remain a topic of debate, the two primary theories are volume increase theory [8,36,14] and crystallization pressure theory [17,84,85]. The crystallization pressure mechanism provides a direct way to calculate the force required for expansion. However, accurately computing this pressure at the pore scale requires a microscopic model that explicitly accounts for pore structures and connectivity, making it complex and computationally demanding. On the other hand, theoretical models based on volume increase theory have demonstrated their ability to predict expansion effectively, particularly in the later stages of ESA [13,86]. Given that the present study focuses on the interaction between sulfate attack and calcium leaching—while also adopting a mesoscopic model with a randomly distributed porosity field that does not explicitly resolve detailed pore structures—the volume increase theory is a more suitable choice.

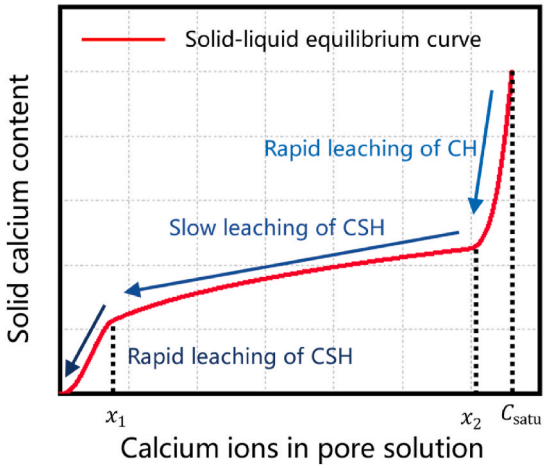


Fig. 3. Schematic representative of Solid-liquid equilibrium curve.

Assuming that solid volume increase is mainly caused by ettringite formation, the volumetric variation caused by **Eqs. (33-35)** can be subsequently determined according to literature:

$$\frac{\Delta V_i}{V_i} = \frac{M_{AFt} - M_i - p_i M_{gyp}}{M_i + p_i M_{gyp}} \tag{46}$$

where M_{AFt}, M_i and M_{gyp} represent the molar volume of ettringite, calcium aluminate phases and gypsum respectively (m^3/mol); p_i is the stoichiometric coefficient of gypsum for chemical reactions in **Eqs, (33-35)**. The specific values for each reactant in this study are shown in Table 1. The overall volume variations caused by ettringite precipitation can be given as:

$$\left(\frac{\Delta V}{V}\right)_{AFt} = a_s C^{react}_{CA} \text{ with } a_s = \sum_{i=1}^{3} \frac{\Delta V_i}{V_i} M_i \lambda_i \tag{47}$$

where C^{react}_{CA} is the total amount of reacted equilibrium calcium aluminate phases that form ettringite, $C^{react}_{CA} = C_{CA0} - C_{CA}$ and C_{CA0} is initial molar concentration of CA (mol/m^3); a_s is the summation of volume change per mole of ettringite formation.

Calcium leaching reduces the solid volume by dissolving CH and decalcifying C-S-H, leading to increased porosity. However, due to the amorphous nature and variable stoichiometry of C-S-H gel, accurately quantifying the volume change as a function of progressive decalcification remains challenging. To address this, the dissolved amounts of CH and C-S-H can be determined using the solid-liquid equilibrium curve, allowing the solid volume loss caused by leaching to be expressed as:

$$\left(\frac{\Delta V}{V}\right)_{Leach} = \left(C^{S}_{Ca^{2+},0} - C^{S}_{Ca^{2+}}\right) V_{CH} \tag{48}$$

where V_{CH} is the molar volume of the CH (3.3×10^{-5} m^3/mol); $C^{S}_{Ca^{2+},0}$ is the initial amount of calcium before leaching, and equals to the sum of initial concentration of calcium hydrate of CH, C_{CH0} and C-S-H, C_{CSH0}. In summary, the total variation of random porosity field under the combined sulfate attack and calcium leaching can be determined by:

$$\varnothing(x,y) = \varnothing_0(x,y) - \left(\frac{\Delta V}{V}\right)_{AFt} + \left(\frac{\Delta V}{V}\right)_{Leach} \tag{49}$$

where $\varnothing(x,y)$ and $\varnothing_0(x,y)$ are the updated and initial porosity filed, respectively. The effect of porosity evolution on ionic diffusion coefficient (H_1) can be determined by using the modified Kozeny-Carman relationship [18]:

$$H_1(\varnothing) = \left(\frac{\varnothing}{\varnothing_0}\right)^3 \left(\frac{1-\varnothing_0}{1-\varnothing}\right)^2 \tag{50}$$

Considering the random porosity field of cementitious materials, the

Table 1
Volume change for each reaction [14].

Chemical reaction	Reactant	Volume change
(33)	C_3A	1.31
(34)	C_4AH_{13}	0.48
(35)	$C_4A\bar{S}H_{12}$	0.55

influence of porosity evolution on the diffusivity of the porous medium varies among different local regions. In the present study, the pore structure is not explicitly modelled; instead, the effects of heterogeneous pore structure characteristics on the ESA process are represented through the combined consideration of a random porosity field and porosity evolution, providing a statistical description of heterogeneity. Future work will focus on incorporating multi-scale pore structure characterization and explicit pore network modeling to further enhance the understanding of the degradation process.

2.3.4. Effect of mechanical damage on transport properties

The mechanical damage during the ESA is mainly attributed to the formation of expansion products. The change in solid volume leads to development of strain and microcrack, which further influence the ionic diffusivities of porous medium. Based on the quantified porosity variations in Section 2.3.3, the expansive volume strain filed $\varepsilon_v(x,y)$ caused by combined sulfate attack and calcium leaching can be calculated as:

$$\varepsilon_v(x,y) = \left(\frac{\Delta V}{V}\right)_{\mathrm{AFt}} - \left(\frac{\Delta V}{V}\right)_{\mathrm{Leach}} - f\varnothing_0(x,y) \tag{51}$$

where f represents the buffer coefficient, which characterizes the fraction of initial porosity that can accommodate expansion without inducing stress. This parameter is typically less than 1, as ettringite, with its needle-like structure, begins to generate stress as soon as its ends make contact with the pore walls, even before the pore is completely filled [85]. Empirically, f is generally taken within the range of 0.05 to 0.4 [36,60], and a value of 0.23 was selected in this study according to the fitting results mentioned in literature [39]. Assuming that the material is isotropic, uniaxial strain is calculated as:

$$\varepsilon(x,y) = \frac{\varepsilon_v(x,y)}{3} \tag{52}$$

As for the expansion deformation, the output result of model is the linear strain of different local regions. So, the expansion deformation of whole specimen can be calculated by the homogenization of linear strain of each local region, as:

$$\varepsilon_l = \frac{\iint \varepsilon(x,y)\mathrm{d}x\mathrm{d}y}{L_x L_y} \tag{53}$$

where L_x and L_y is the specimen size at x and y direction, respectively. Expansion induced microcracks will increase ionic diffusivities [87]. According to approach taken by other researchers, the effect of mechanical damage on transport properties (H_2) can be calculated as:

$$H_2(C_d) = \left(1 + \frac{32}{9}C_d\right) + D_p \tag{54}$$

$$D_p = \begin{cases} 0 & C_d < C_{dc} \\ (C_d - C_{dc})^2/(C_{dec} - C_d) & C_{dc} \le C_d < C_{dec} \end{cases} \tag{56}$$

where C_d is the crack density; C_{dc} and C_{dec} are two percolation thresholds by Sarkar et al. [36] to quantify the conduction percolation and rigidity percolation respectively. They are numerical determined to be 0.182 and 0.712 by Charlaix [88] and Sornette [79], respectively. k is the upper limit of crack density and is adopted as 0.16; $\varepsilon_{\mathrm{th}}$ is the threshold strain signifying crack initiation (4×10^{-5}); D_p is the diffusivity in the percolation regime.

2.3.5. Governing equation for diffusive-reactive process

In the present work, the transport process in a saturated porous medium is considered to be driven by concentration gradient and the potential gradient [89–91]. The time-dependent ionic concentrations can be derived with the consideration of reaction terms caused by chemical reactions, as shown in Eq. (57).

$$\frac{\partial C_i}{\partial t} = -\nabla \cdot J_i + S_i \tag{57}$$

where C_i is the concentration of species i in solution; S_i is the source term; J_i is the ionic flux, given by:

$$J_i = -D_i \nabla C_i - D_i C_i \frac{z_i \mathrm{F}}{\mathrm{R}T} \nabla \Phi \tag{58}$$

where D_i is the diffusion coefficient of ion i in solution; z_i is the charge number carried by i-th ion, such as Na^+, K^+, Ca^{2+}, SO_4^{2-}, OH^-, F is the Faraday constant (96488.46 C/mol); R is the ideal gas constant (8.314 J/mol/K); T is the absolute temperature; Φ is the electrostatic potential. Note that ionic species in pore solution are not always compliant with the electric neutrality hypothesis, and the coexistence of various ionic species will result in an electrochemical coupling effect. In this case, the traditional Laplacian equation, $\nabla^2\Phi = 0$, used to solve electrostatic potential distribution under the electric neutrality assumption should be replaced by the more rigorous Poisson equation based on the constitutive electrochemical law as [92–94]:

$$\nabla^2 \Phi = -\frac{1}{\varepsilon_0 \varepsilon_r}\left(\mathrm{F}\sum z_i C_i\right) \tag{59}$$

where ε_0 is the vacuum permittivity (8.854×10^{-12} F/m); ε_r is the dielectric constant of water (78.3), $\mathrm{F}\sum z_i C_i$ determines the charge volume density caused by charge imbalance in pore solution ($C{\cdot}m^{-3}$). Electrostatic potential at the specimen surface is explicitly set to zero as a boundary condition. Substituting chemical reaction term derived in Section 2.3.1 and Section 2.3.2 into **Eq. (57)**, the diffusive-reactive equations for various ions can be given as follows:

$$\begin{cases} \dfrac{\partial C_{\mathrm{SO_4^{2-}}}}{\partial t} = \nabla \cdot \left(D_{\mathrm{SO_4^{2-}}} \nabla C_{\mathrm{SO_4^{2-}}} + D_{\mathrm{SO_4^{2-}}} C_{\mathrm{SO_4^{2-}}} \dfrac{z_{\mathrm{SO_4^{2-}}} \mathrm{F}}{\mathrm{R}T} \nabla \Phi\right) - k_1 C_{\mathrm{SO_4^{2-}}} C_{\mathrm{Ca^{2+}}} & i = \mathrm{SO_4^{2-}} \\ \dfrac{\partial C_{\mathrm{Ca^{2+}}}}{\partial t} = \nabla \cdot \left(D_{\mathrm{Ca^{2+}}} \nabla C_{\mathrm{Ca^{2+}}} + D_{\mathrm{Ca^{2+}}} C_{\mathrm{Ca^{2+}}} \dfrac{z_{\mathrm{Ca^{2+}}} \mathrm{F}}{\mathrm{R}T} \nabla \Phi\right) - k_1 C_{\mathrm{SO_4^{2-}}} C_{\mathrm{Ca^{2+}}} - \dfrac{\partial C^S_{\mathrm{Ca^{2+}}}}{\partial t} & i = \mathrm{Ca^{2+}} \\ \dfrac{\partial C_i}{\partial t} = \nabla \cdot \left(D_i \nabla C_i + D_i C_i \dfrac{z_i \mathrm{F}}{\mathrm{R}T} \nabla \Phi\right) & i = \text{others} \end{cases} \tag{60}$$

$$C_d = \begin{cases} k(1 - \varepsilon_{\mathrm{th}}/\varepsilon)^{2.3} & \varepsilon > \varepsilon_{\mathrm{th}} \\ 0 & \varepsilon < \varepsilon_{\mathrm{th}} \end{cases} \tag{55}$$

with the consideration of both porosity evolution and mechanical damage, the time- and space-dependent ionic diffusivity can be calculated by the initial ionic diffusivity, D_k^0, multiplied with H_1 and H_2 as:

Table 2
Chemical compositions of cement and fly ash (mass fraction %).

Ref	Material	CaO	SO_3	Al_2O_3	Fe_2O_3	SiO_2	L.O.I.
[15]	Cement1	65.0	2.05	4.9	2.8	21.2	0.86
	FA1	2.2	0.4	25.5	4.3	62.0	2.22
[16]	Cement2	63.20	2.88	4.25	3.49	20.10	0.86
	FA2	3.38	0.60	20.40	8.66	53.50	2.20

Table 3
Mixture proportion for mortar specimens (kg/m^3).

Ref	Specimen	Cement	Water	Fly ash	Aggregate	Fly ash ratio
[15]	FA1-20%	80	40	20	0	20%
	FA1-40%	60	40	40	0	40%
	FA1-60%	40	40	60	0	60%
[16]	FA2-0%	515	257	0	1544	0%
	FA2-10%	515	257	52	1483	10%
	FA2-20%	515	257	103	1422	20%
	FA2-30%	515	257	154	1361	30%

$$D_k = H_1(\varnothing)H_2(C_d)D_k^0 \tag{61}$$

3. Model validation

In this paper, the proposed modelling framework is validated by comparing its results with experimental data from Papadakis [16], Yu et al. [17] and Liu et al. [21] covering hydration products, expansion deformation of OPC mortar, and blended cement pastes. The validation encompasses a range of conditions, including different external fly ash replacement levels, sulfate concentrations and specimen sizes, to ensure comprehensive comparison.

3.1. Validation of cement-fly ash blend hydration model

In this section, experimental results from the hydration of cement–fly ash blends [16] and [15] are used to validate the hydration model, including the reaction degree of fly ash, phase content and porosity. The chemical compositions of the cements and fly ashs are provided in Table 2, while the mixture proportions with varying fly ash contents are listed in Table 3. In Ref. [15] study, fly ash was used to replace the cement at three levels—20%, 40%, and 60% weight of cement with water to powder ratio of 0.4. Specimens were kept for 7, 28, 56, 91, 180, 270 and 360 days at 20 °C in sealed bottles. The reaction degree of fly ash and calcium hydroxide (CH) content were measures at each time. In Ref. [16] study, a volume of mortar was chosen as the standard reference. Fly ash was used to replace the aggregate volume at three levels—10%, 20%, and 30% weight of cement. All specimens were cured under sealed conditions at 20 °C. The CH content, chemically bound water content, and porosity were measured at 3, 7, 14, 28, 49, 112, 182, and 364 days after casting.

Firstly, Fig. 4 compares the predicted and experimentally measured reaction degree of fly ash and CH content reported in Ref. [15]. As shown in Fig. 4(a), the results predicted by the modified hydration model agree well with the experimental trend that the reaction degree of fly ash increases with a lower fly ash replacement ratio, indicating that a higher fly ash replacement level suppresses the pozzolanic reaction. With the consideration of time-dependent pozzolanic processes, the predicted CH contents also show good agreement with the experimental results, as illustrated in Fig. 4(b), exhibiting an initial increase followed by a subsequent decrease.

Furthermore, the comparison between the predicted and tested CH content in Ref. [16] study over time is presented in Fig. 5. The predicted results show good agreement with the experimental data. In the hydration of Portland cement, the CH content increases progressively and eventually reaches a steady state, as illustrated in Fig. 5(a). In contrast, for cement–fly ash blends, the CH content is governed by two competing processes: CH generation from Portland cement hydration and CH consumption through the pozzolanic reaction. As a result, the CH content initially increases but subsequently decreases over time. With higher fly ash content, the overall CH content declines, as observed in Fig. 5(b–d). Correspondingly, due to the pozzolanic activity of the fly ash, the formation of CSH is enhanced. Although the CSH content is not directly measured, its predicted evolution is governed by the validated fly ash reaction degree and CH consumption, providing an indirect but physically consistent basis for assessing CSH formation.

The evolution of porosity as a function of hydration time is illustrated in Fig. 6. The calculated results show good agreement with the experimental data. As hydration progresses, porosity decreases steadily. As shown in the figure, the incorporation of fly ash can reduce porosity; however, the extent of fly ash addition has a relatively minor influence on the final porosity.

3.2. Validation of expansion strain: varying specimen sizes and sulfate concentration

Before validating the model against expansion behavior of fly ash-blended cement pastes, the expansion response of ordinary Portland cement (OPC) mortar is first examined. This preliminary validation step aims to assess the model's capability to capture the influence of key external factors—specifically sulfate concentration and specimen size—on expansion behavior under sulfate attack. Although the ultimate focus of this study lies in fly ash-blended systems, validating the model with OPC mortar provides a benchmark and ensures that the fundamental sulfate-related degradation mechanisms are accurately represented, thereby reinforcing the reliability of subsequent predictions for blended systems.

The modelled results were compared with experimental axial

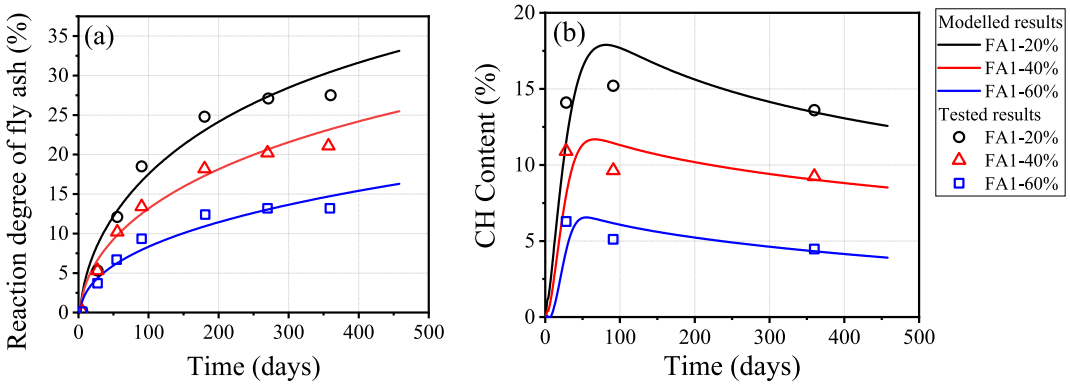


Fig. 4. Comparison of predicted and tested (a) reaction degree of fly ash and (b) CH content.

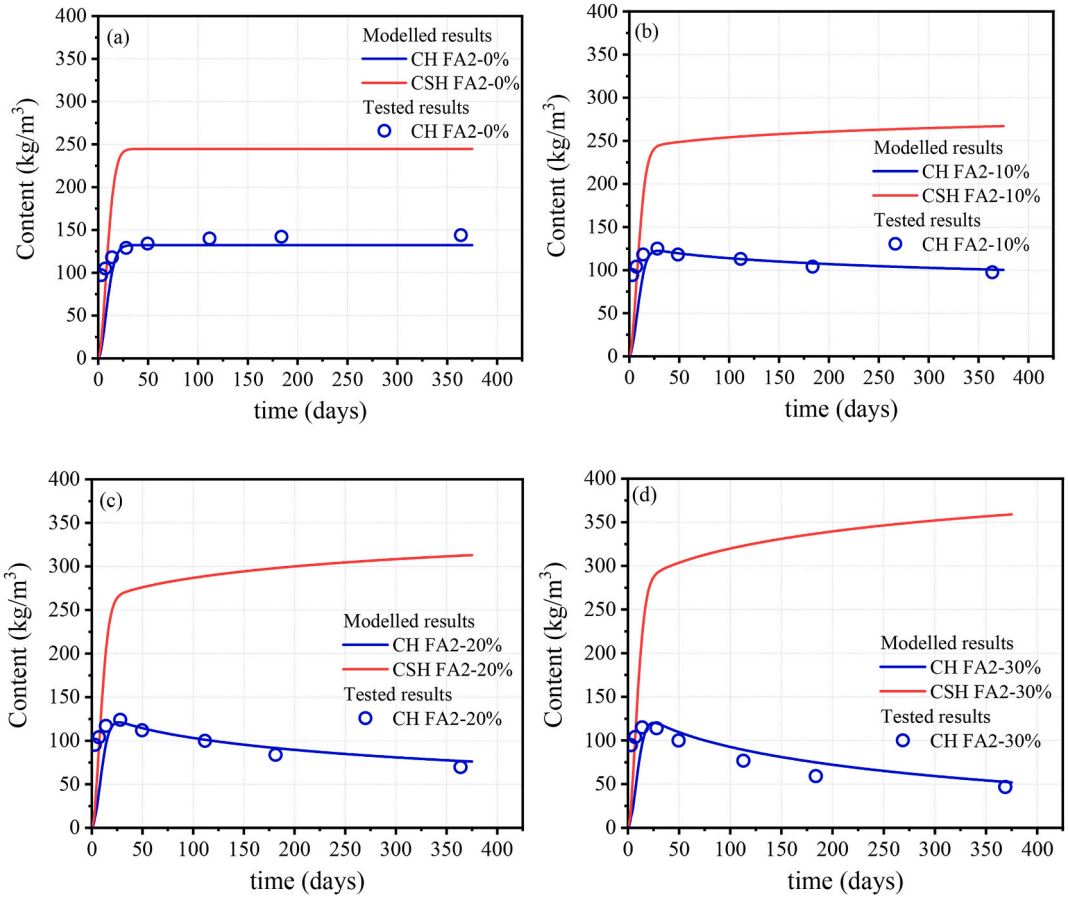


Fig. 5. Comparison of calculated and tested phase contents (a) 0% (b) 10% (c) 20% (d) 30%.

deformation data from Yu et al. [17]. Mortar specimens of three different sizes—10 × 10 × 160 mm, 20 × 20 × 160 mm, and 40 × 40 × 160 mm—were cast using ordinary Portland cement (CEM I 52.5), with its chemical composition provided in Table 4. A water-to-cement ratio of 0.55 was used, and sand-to-cement ratio is 3. In Yu's work, to assess the effect of specimen sizes on expansion deformation, each series was submerged in a 3 g/L (21.1 mol/m^3) sodium sulfate solution at 293 K. Additionally, for the 20 × 20 × 160 mm series, specimens were exposed to sulfate solutions of varying concentrations—3 g/L (21.1 mol/m^3) and 30 g/L (211 mol/m^3)—to evaluate the influence of sulfate concentration on expansion deformation.

Since Yu's study used cement mortars rather than concrete, the meso-scale model established in this section does not differentiate between sand and the ITZ phases. The average porosity of the cement mortar was measured at 13%. The values of a and b were assumed to be 0.005 m, with a coefficient of variation (CV) of 0.1. The randomly generated porosity fields for the three different specimen sizes are shown in Fig. 7. Other parameters used in the model are listed in Table 5.

Fig. 8(a) compares the modelled and experimental expansion of mortar bars of different sizes immersed in a 3 g/L Na_2SO_4 solution, while Fig. 8(b) presents the comparison for specimens of the same size exposed to either 3 g/L or 30 g/L Na_2SO_4. The results clearly show that smaller specimens experience greater expansion. This behavior is mainly attributed to the higher surface-to-volume ratio of smaller specimens, which leads to a more rapid accumulation of sulfate ions within the material over the same exposure duration. In addtion, reuslts also show higher sulfate concentrations lead to increased expansion. The increased sulfate concentration promotes earlier formation of expansive reaction products and stress concentration. The modelled results demonstrate good agreement with the experimental data. In the early stage, expansion increases gradually as expansive products form and fill the pores. After a period of sulfate immersion, the expansion accelerates with continued exposure. This indicates that a portion of the porosity must be filled before significant volumetric strains develop. Since the research primarily investigates the expansion strain along the axial direction, a 2D meso-scale model is sufficient to capture the key characteristics of this process, while significantly reducing computational complexity compared to a 3D model.

Fig. 8(c) shows the results from Rozière et al. [19], where mortar specimens of different sizes were immersed in sulfate solution for a period of time. The results clearly indicates that smaller specimens exhibit through cracks earlier than the larger ones (marked by yellow circles), while the 40 × 40 × 160 mm -sized specimens only show delamination at the specimen edges (marked by blue circles). The experimental results also found that the sulfate content in the solids near the surface are reduced due to leaching (since all sulfate-bearing minerals in the system contain calcium), so the maximum expansion force is likely to occur just a few millimeters below the surface, where cracks initiate first (as indicated by the red dashed lines in the figure).

Fig. 9 shows the modelled strain distribution $\varepsilon(x, y)$ after 360 days of exposure to a 3 g/L Na_2SO_4 solution for meso-scale models with and without a random porosity field. It can be observed that, regardless of whether the random porosity field is considered, the strain values decrease as the specimen size increases. For the 40 × 160 mm size, strain is concentrated at the four corners of the specimen, as shown by the blue circles in Figs. 9(c-1, 2). Additionally, as observed experimentally, modelled results also show the maximum expansion force occurs about one to 2 mm from the surface, as indicated by the red dashed lines in Figs. 9(c-1, 2). In the model with random porosity field, the strain distribution in the modelled results becomes more irregular. For the 20 ×

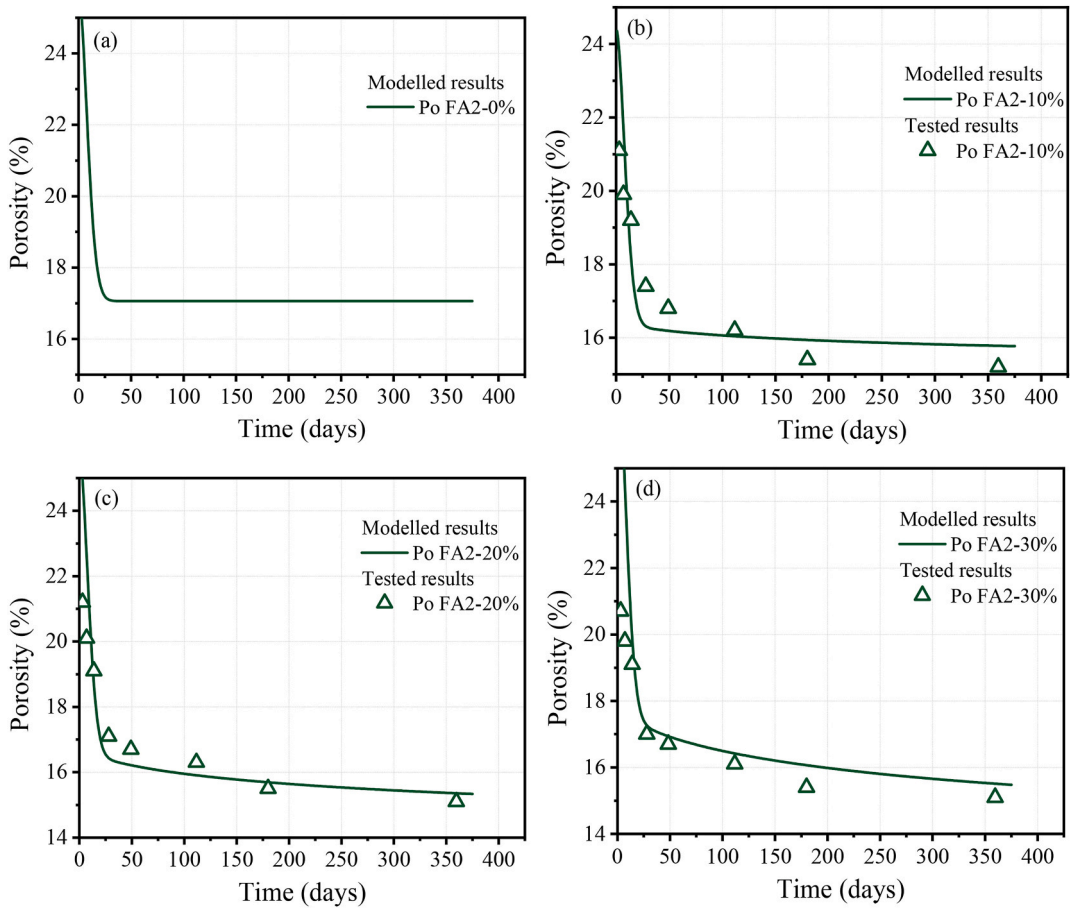


Fig. 6. Comparison of calculated and tested results of porosity (a) 0% (b) 10% (c) 20% (d) 30%.

Table 4
Chemical composition of ordinary Portland cement used by Yu et al. [17].

Chemical Compositions	SiO_2	Al_2O_3	CaO	MgO	SO_3	Fe_2O_3	Others
Mass(%)	21.01	4.63	64.18	1.82	2.78	2.60	1.26

160 mm size, the model can capture the formation of through cracks, as seen in the red circle in Figs. 9(b–1). However, in Figs. 9(b–2), only delamination around the edges is observed, which clearly does not match the actual situation shown in Fig. 8(c). This emphasizes the importance of considering random porosity distribution when modeling ESA in cementitious materials to more accurately reflect real degradation behavior.

3.3. Validation of expansion strain: varying fly ash replacement

Liu et al. [21] experimentally studied the effects of fly ash contents on cement pastes under external sulfate attack and measured the resulting expansion strains. In the experiment, the research specimens were the hardened cement paste with size 20 × 20 × 80 mm, prepared using ordinary Portland cement (42.5 R) and low-calcium fly ash (chemical composition provided in Table 6). Cement pastes samples were prepared with replacement of 0%, 20% and 40% fly ash by weight of cement. The detailed mix proportions are listed in Table 7. After demolding, the specimens were cured at 298 K for 28 days, followed by immersion in a 5% Na_2SO_4 solution at 298.15 K for a duration of 1100 days.

Based on the chemical composition and mix proportions, the mass of hydration products in different samples was calculated using the hydration model shown in Fig. 10. As the replacement level of cement with fly ash increased, the contents of both CH and CSH gradually decreased. The boundary concentrations were set according to the experimental exposure solutions by converting the weight percentage (5%) to molar concentration (352 mol/m^3). Parameters used in the model are listed in Table 8.

The modelled and tested expansion strain in cement pastes with different fly ash content after 1100 days exposure is compared in Fig. 11. The modelled results align with the experimental data. During the initial ~120 days, negligible expansions were observed in all specimens immersed in the 5% Na_2SO_4 solution, primarily due to the initial pore-filling process. Thereafter, expansion accelerated with prolonged exposure. The results further demonstrate that increasing the replacement level of cement with low-calcium fly ash effectively reduces expansion strain. This reduction is mainly attributed to the decreased CH and CA contents, which limit the formation of expansive products, as well as to porosity refinement at higher replacement levels that slows sulfate diffusion, as shown in Fig. 10 and Table 8. However, between approximately 200 and 600 days, the model slightly underestimates the measured expansion strains. This discrepancy may be partly attributed to the assumption of a constant buffer coefficient f, which represents the fraction of porosity available to accommodate expansive products without inducing stress. In practice, the development of microcracking progressively reduces the material's buffering capacity. As a result, f is likely to evolve with time and damage. Treating f as a fixed parameter may therefore oversimplify the degradation process and contribute to the underestimation of mid-term expansion. Further refinement of this assumption will be considered in future work.

Taking the FA20% sample as an example (cement mortar with $\varnothing_a$ = 13% and different CV exposed to 3 g/L Na_2SO_4 solution after 360 days),

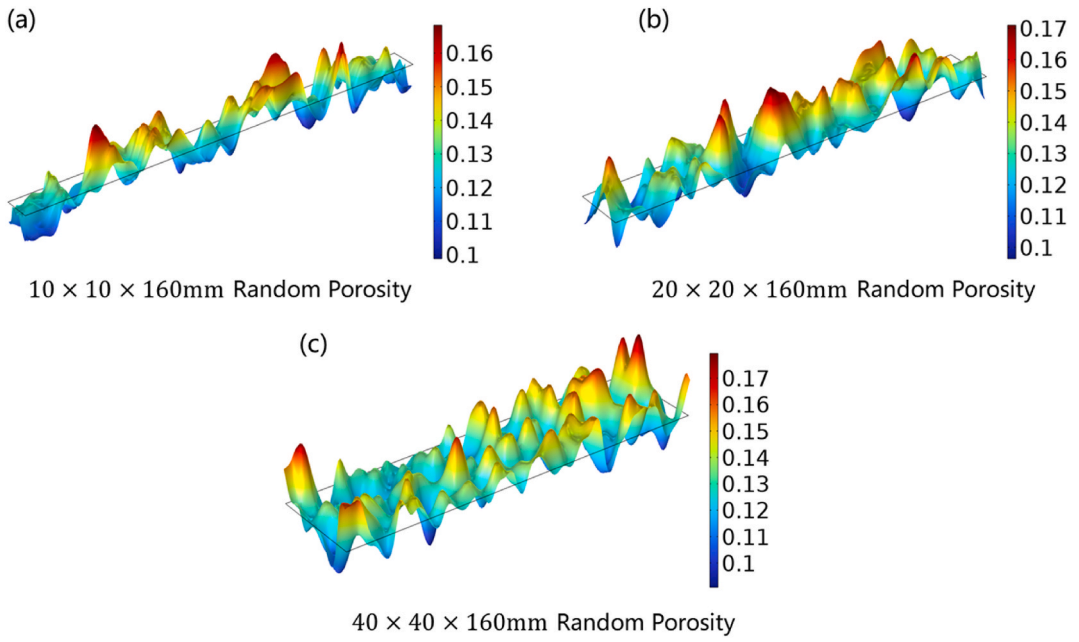


Fig. 7. Modelled random porosity field for different sizes of mortar specimens.

Table 5
Parameters used in the model.

Parameters	Symbols	Value	Reference
Solid initial concentrations	C_{CA0} (mol/m^3)	121	Calculated by hydration model
	C_{CH0} (mol/m^3)	2087	
	C_{CSH0} (mol/m^3)	870	
Stoichiometric coefficient	q	2.15	Calculated
Diffusion coefficients	$D_{Ca^{2+}}$ (m^2/s)	2.0×10^{-11}	[18]
	$D_{SO_4^{2-}}$ (m^2/s)	2.7×10^{-11}	
Volume change coefficient	a_s (m^3/mol)	3.07×10^{-4}	[19]
	k	0.66	
Random Porosity field	$\varnothing_a$ (%)	13	Tested
	CV	0.1	[20]

Fig. 12 further explores the influence of the coefficient of variation (CV) on the expansion strain field. As CV increases, the porosity field becomes rougher and more heterogeneous, leading to a more complex stress field and a higher likelihood of through-crack formation. The core region is also more significantly affected. Fig. 13 shows that an increase in the initial CV ultimately results in higher expansion strain. This phenomenon may be attributed to the uneven initial porosity, which limits the pore space available for expansive reaction products. As a result, expansion strain develops earlier, promoting crack formation, which in turn accelerates sulfate diffusivity. These comparisons also further highlight the importance of considering heterogeneity in predictive modeling. Beisdes, to some extent, the distribution of the porosity field reflects the overall quality of the mortae - the more uniform it is, the better the quality. The modelled results indicate that poorly constructed or highly uneven mortar is more susceptible to degradation caused by ESA.

4. Results and discussion

In this section, a parametric analysis will be conducted to evaluate the impact of different model settings on the results, as well as the effects of initial chemical composition of fly ash on ESA resistance. To provide guidance on the selection of fly ash for ESA-resistant cementitious materials, the relationships between fly ash mineral indicators and ESA performance are also analyzed.

4.1. Influence of model settings on modelled results

The model, with size 20 × 80 mm and 20% fly ash replacement, is exposed to 5% sodium sulfate solution for a duration of 1100 days, consistent with the model parameters used for validating Liu et al.'s experimental results in Section 3.3. Fig. 14 shows the modelled results with and without considering calcium leaching, the sulfate-induced acceleration of calcium leaching, and porosity variations in model settings. As shown in Fig. 14(a), the expansion will be overestimated if porosity changes are not taken into consideration. Dissolution of CH and decalcification of C-S-H increase porosity, allowing pores to fill with more expansion products. If the increased porosity at early stage is not considered, expansion strain develops at earlier time, finally resulting in the overestimated expansion results. Correspondingly, Fig. 14(b) shows that ignoring porosity changes also leads to an overestimation of sulfate ion penetration. This is primarily due to the underestimated damage resistance of the material, and severe damage facilitates faster transport of sulfate ions.

Calcium leaching typically occurs in conjunction with sulfate attack, with both processes interacting dynamically. Fig. 14(a) indicates neglecting calcium leaching results in significantly lower expansion compared to the proposed model that incorporates all influencing factors. This discrepancy can be attributed to the reduced concentration of calcium ions, which plays a crucial role in governing the chemical reactions involved. In Fig. 14(b), the predicted sulfate concentration profile without calcium leaching closely matches the boundary concentration. In the absence of sufficient calcium, sulfate ions undergo limited reaction and primarily diffuse into the matrix, eventually approaching equilibrium.

Furthermore, Fig. 14(a) indicates that ignoring the sulfate-induced acceleration of calcium leaching leads to an underestimation of the predicted results. As shown in Fig. 15(a and b), the solid-liquid equilibrium curves differ among free water and 5% Na_2SO_4 solution. With increasing sulfate concentration, calcium leaching is accelerated. As the

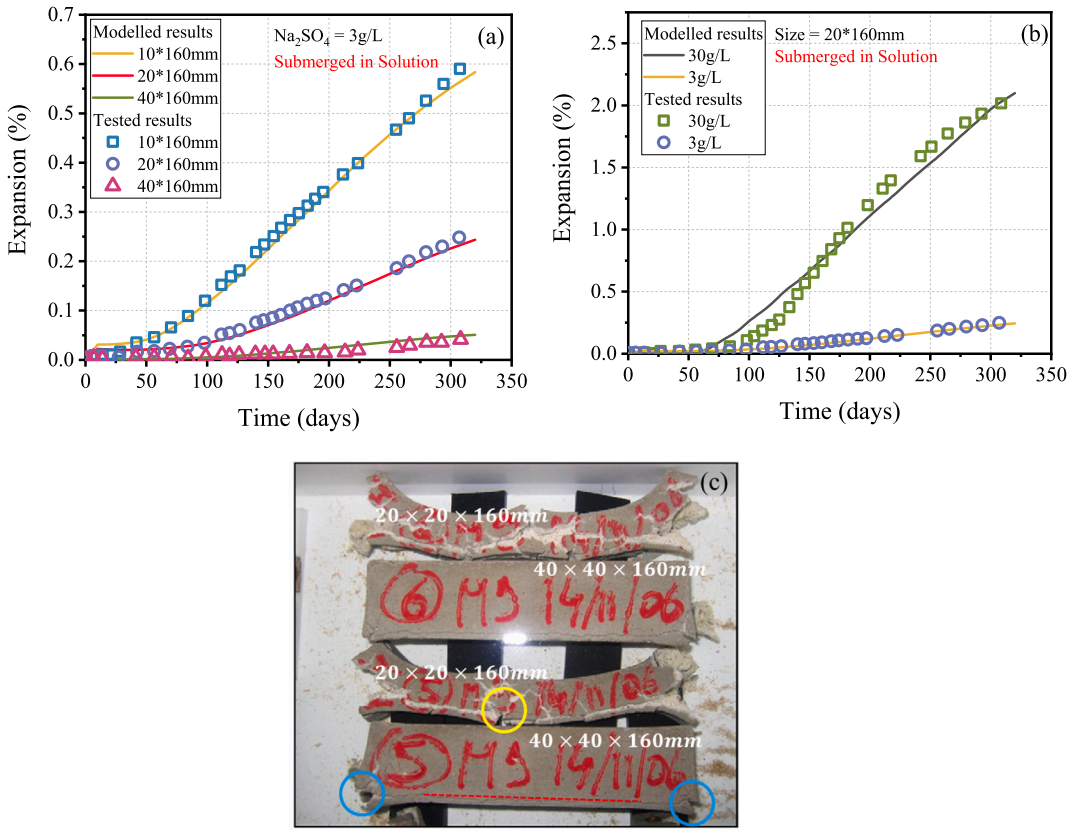


Fig. 8. The comparison of expansion strain (a) different sizes (b) same size exposed to different solutions (c) Mortar specimens done by Rozière et al. [19].

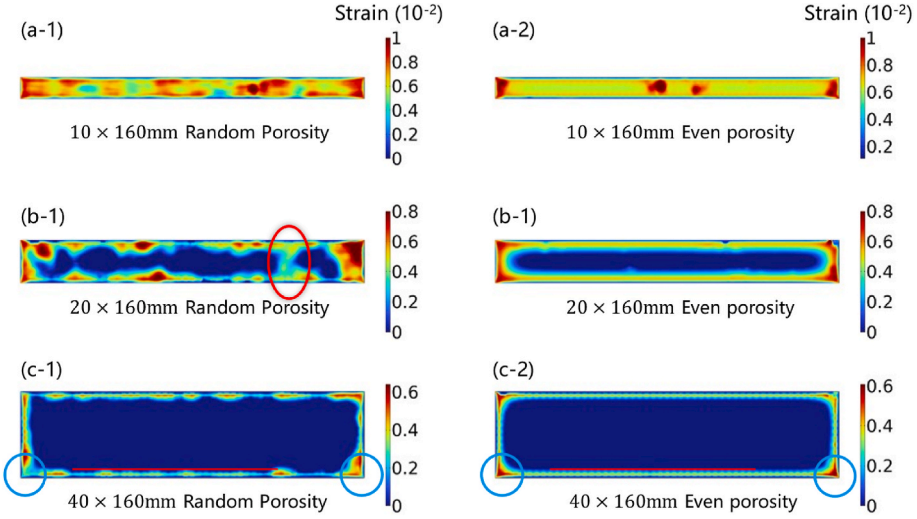


Fig. 9. Modelled expansion strain field (a-1, 2) 10 × 160 mm (b-1, 2) 20 × 160 mm (c-1, 2) 40 × 160 mm.

Table 6
Chemical composition of ordinary Portland cement and fly ash used by Liu et al. [21].

	CaO	SO_3	Al_2O_3	Fe_2O_3	SiO_2	L.O.I.
Cement	61.14	2.28	5.15	3.31	21.95	2.02
Fly ash	3.85	0.39	20.21	11.73	57.29	1.51

Table 7
Compositions of the cement paste mixtures.

Specimen	Cement	Water	Fly ash	w/c
FA0%	1630	489	0	0.3
FA20%	1304	489	326	
FA40%	978	257	652	

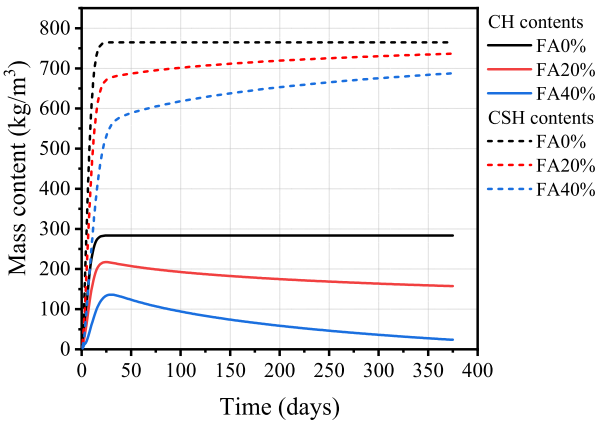


Fig. 10. Mass content of CH and CSH in cement pastes with varying fly ash replacements.

Table 8
Parameters used in the model.

Parameters	Symbols	Value FA0%	Value FA20%	Value FA40%	Reference
Solid initial concentrations	C_{CA0} (mol/m^3)	280	229	170	Calculated
	C_{CH0} (mol/m^3)	3826	2923	1833	
	C_{CSH0} (mol/m^3)	2233	1974	1606	
Stoichiometric coefficient	q	2.25	2.19	2.15	
Diffusion coefficients	$D_{Ca^{2+}}$ (m^2/s)	1.7×10^{-12}	Based on porosity reduction Eq. (50)		[22,18]
	$D_{SO_4^{2-}}$ (m^2/s)	2.3×10^{-12}			
Volume change coefficient	α_s (m^3/mol)	1.6×10^{-4}			[19]
	k	0.66			
Random Porosity field	$\varnothing_a$ (%)	36.06	15.42	14.39	Tested
	CV	0.1 for all samples			[20]

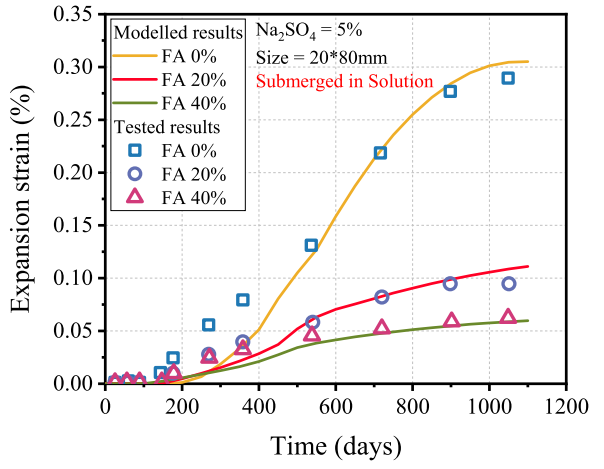


Fig. 11. The comparison of expansion strain in fly ash blended cement paste exposed to 5% Na_2SO_4 solution.

chemical reactions progress, the dissolution rates of CH and C-S-H in sulfate solutions will be higher than in free water, continuously replenishing calcium ions. In addition, sulfate-accelerated leaching primarily increases porosity at early ages, which in turn affects the timing of expansion. As shown in Fig. 15(c and d), neglecting this acceleration reduces both the reaction extent of calcium aluminate (CA) and the dissolution of solid calcium. The former limits the formation of expansive products, while the latter suppresses porosity increase, jointly altering the expansion development. However, as shown in Fig. 14(a), for fly ash–blended cementitious materials, the former effect dominates, resulting in an overall reduction in expansion. Despite these model settings, it should be noted that the present model has several limitations. These include the assumption of uniform temperature, the adoption of a two-dimensional framework instead of a full three-dimensional representation, and the lack of explicit calibration of diffusivity parameters. These aspects require further investigation in future work.

4.2. *Influence of initial chemical composition of fly ash on ESA*

Compared to OPC, the mineral composition of fly ash is less stable, which may lead to differences in the hydration products (e.g., CH, C-S-H, and CA contents), ultimately affecting the material's resistance to ESA. To investigate the influence of mineral composition on this performance, this study collected data on 10 real low-calcium fly ashes from the literature, as listed in Table 9. Using the proposed numerical model, their incorporation into cement paste at replacement levels of 10%, 20%, and 30% were simulated. After 28 days of curing, the samples were subjected to immersion in a 5% Na_2SO_4 solution for 1000 days to assess their performance. The cement mineral compositions and other relevant parameters used in the model were consistent with those described in Section 3.3.

As shown in the Table 9, although all ten samples are classified as low-calcium fly ash, their calcium content varies significantly, ranging from 1.55% to 7.8%. The contents of Al_2O_3 and SiO_2 also exhibit variations exceeding 10%. As discussed in the hydration section, even minor differences in mineral composition can influence the final hydration products. The key input parameters and the corresponding expansion results for the 30 modelled cases are presented in Table 10. It is evident that, despite having the same replacement levels, the final expansion results differ considerably. Therefore, the fly ash replacement ratio alone is insufficient to predict its effect on the performance of blended cement paste.

Fig. 16 presents the modelled expansion strain field with varying initial equilibrium CA contents, solid calcium and porosity. As shown in Fig. 16(a), despite substantial variations in CA content resulting from 10 to 30% fly ash replacement, a clear linear relationship is observed between CA content and expansion strain. Specifically, higher initial CA content leads to a pronounced increase in expansion. In general, the 30% fly ash group demonstrates superior resistance to ESA compared to the 20% group, which in turn outperforms the 10% group. Conversely, although previous studies have reported that elevated total calcium content tends to reduce ESA resistance, Fig. 16(b) indicates that this trend holds only within individual replacement levels, with no consistent correlation observed across the full dataset. This implies that, among the initial mineralogical components, CA content exerts the most dominant influence on expansion behavior. As shown in Fig. 16(c), a decrease in the initial average porosity ultimately results in a higher expansion strain. However, the data exhibit greater scatter compared to the trends observed for CA content. This behavior can be attributed to the dual role of porosity. On the one hand, lower porosity reduces the available space for the precipitation of expansive products, which has been shown to suppress expansion in systems with finer pore structures, as reported by Ran et al. [58]. On the other hand, reduced porosity also hinders sulfate ion transport, thereby limiting the ingress of aggressive species. This competing effect results in a more variable influence on expansion behavior. A grey relational analysis considering seven variables—fly ash content ($\gamma = 0.548$), CA content ($\gamma = 0.816$), CH content ($\gamma = 0.753$), C-S-H content ($\gamma = 0.901$), average porosity ($\varnothing_a$, $\gamma = 0.556$), α_s ($\gamma = 0.574$), and q ($\gamma = 0.700$)—was performed to quantify their relative influence (γ) on the expansion behavior. The sensitivity ranking

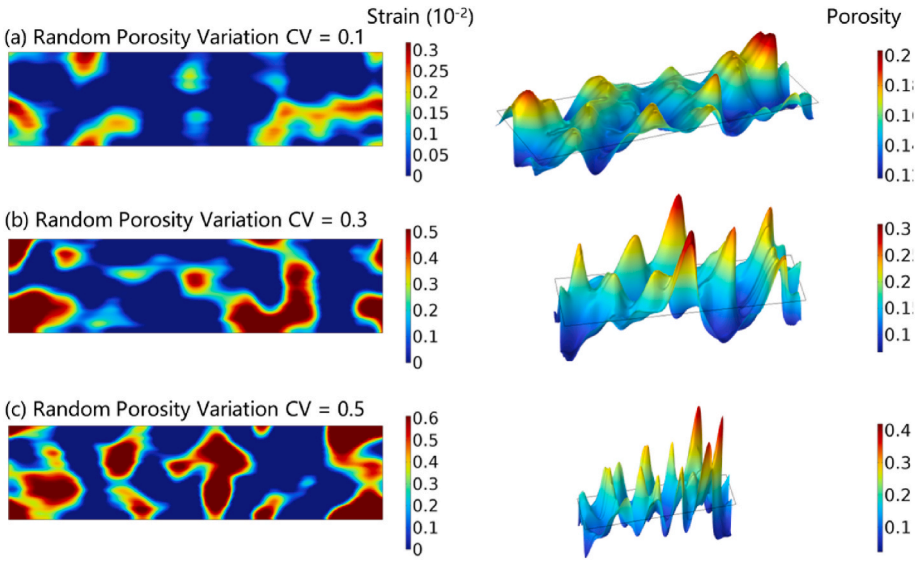


Fig. 12. The modelled expansion strain field in (a) CV = 0.1 (b) CV = 0.3 (c) CV = 0.5.

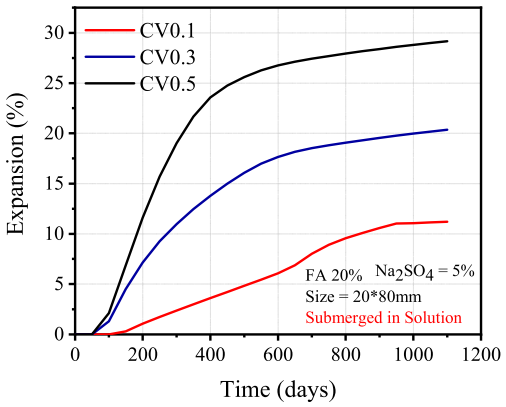


Fig. 13. The modelled expansion strain of cement mortar with different CVs.

indicates that expansion is primarily governed by C-S-H, CA, and CH contents, followed by q, a_s, and $\varnothing_a$, while fly ash replacement level plays a secondary role.

This section explored how the hydration-induced properties of cementitious systems incorporating different types of fly ash affect their resistance to ESA. In the next section, quantitative indicators related to the initial mineralogical composition of fly ash will be analyzed to provide further insight into their correlation with ESA performance, thereby supporting the selection of suitable fly ashes for ESA-resistant applications.

4.3. Relationship between fly ash indicators and ESA performance

In this section, the resistance of belended cementious materials to ESA is evaluated by defining performance index as the ratio of expansion in fly ash–blended systems to that of the control system made with 100% OPC, as described below.

$$\text{Performance index} = \frac{\text{Expansion in blended systems}}{\text{Expansion in control system}} \tag{62}$$

Previous studies have demonstrated that the oxide composition of fly ash—including silica, alumina, iron oxide, and calcium oxide—as well as the proportions of amorphous and crystalline phases, can significantly affect sulfate resistance [95]. To quantify this, an R-factor has been proposed as an indicator of sulfate resistance, which incorporates the contents of CaO and Fe_2O_3 in the fly ash. The R-factor is defined by the following equation [96]:

$$R = \frac{\text{CaO}(\%) - 5}{\text{Fe}_2\text{O}_3}\% \tag{63}$$

Fig. 17(a) illustrates the correlation between the performance index and the R-factor based on the data presented in Table 10. Although a

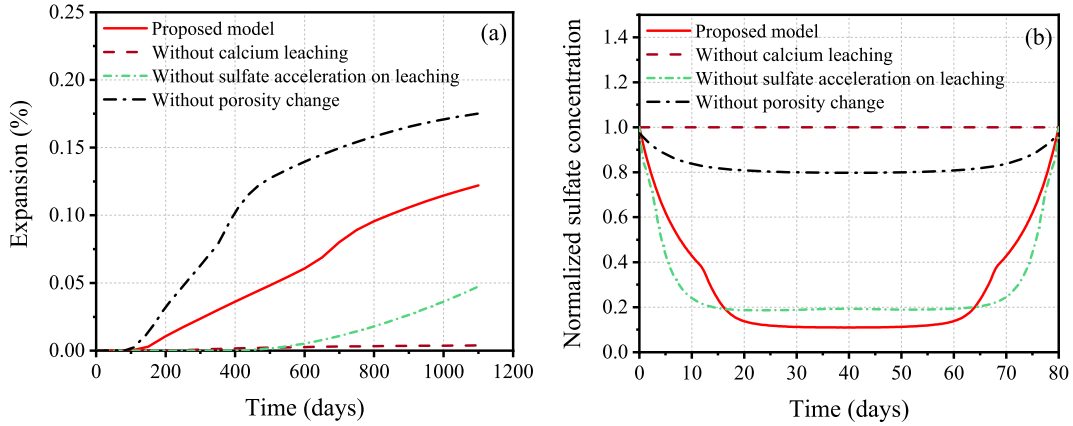


Fig. 14. Submerged in 5% Na_2SO_4 solution with different model setting (a) modelled expansions (b) modelled sulfate concentration distribution after 600 days.

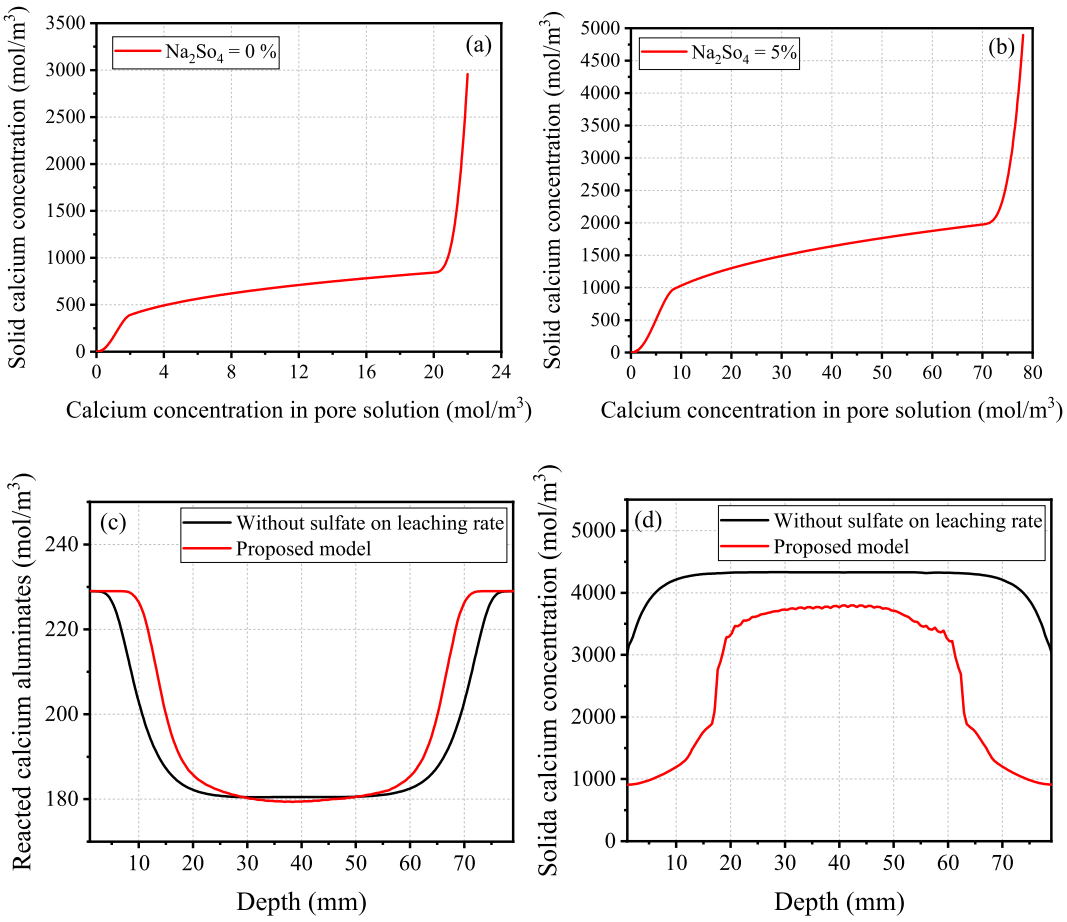


Fig. 15. The solid-liquid equilibrium curves (a) in free water (b) in 5% sulfate solution Phase distribution immersed in 5% sulfate solution (c) Reacted calcium aluminate (d) solid calcium.

Table 9
Chemical composition of 10 types of fly ash reported in literature.

	CaO	SO_3	Al_2O_3	Fe_2O_3	SiO_2	Ref
FA1	3.38	0.6	20.4	8.66	53.5	[16]
FA2	7.47	2.25	18.91	9.3	52.34	[23]
FA3	1.55	0.45	23.4	6.97	58.58	[24]
FA4	2.18	0.48	19.65	10.67	58.85	[25]
FA5	7.5	0.4	20.5	5.6	58.9	[26]
FA6	3.05	0.3	18.97	4.39	66.67	[27]
FA7	2.2	0.4	25.5	4.3	62	[15]
FA8	5.8	0.4	21.7	7.8	54.7	[28]
FA9	2.5	0.4	33.9	4.45	54	[29]
FA10	7.8	0.41	21.9	2.7	57.6	[30]

general trend is observed in which a higher R-factor corresponds to improved resistance to ESA at each fly ash replacement level, the overall data scatter prevents the establishment of a strong statistical correlation. Nevertheless, it is notable that for mixtures with R-factors less than zero, the performance index consistently remains below 80%, suggesting a potential threshold for poor ESA resistance.

Furthermore, several studies [21,97,98] have reported that concrete incorporating fly ash exhibits enhanced sulfate resistance when the CaO/SiO_2 ratio of the fly ash is below 0.25, whereas significantly reduced resistance is observed when the ratio exceeds 0.60. Based on these findings, the relationship between the CaO/SiO_2 ratio and the corresponding sulfate-induced expansion ratio is plotted in Fig. 17(b). In the present study, all CaO/SiO_2 ratios fall below the 0.25 threshold. However, as shown in the figure, some mixtures still exhibit a performance index close to 100%, indicating a high degree of variability. The data appear scattered and do not clearly follow the previously reported 0.25 and 0.60 boundary values. Nevertheless, it is worth noting that most samples with a CaO/SiO_2 ratio below 0.10 correspond to performance indices below 80%, suggesting that lower ratios may be associated with better sulfate resistance within this dataset.

In addition, the indicator proposed by Elahi et al. [31] is also plotted in Fig. 17(c). However, the weak correlation observed also suggests that evaluating fly ash performance based solely on oxide composition is insufficient. This highlights the difficulty in selecting suitable fly ash based purely on its chemical composition. Nonetheless, the analysis indicates that higher fly ash replacement levels (>10%) and lower values of key indicators are generally associated with improved ESA resistance. Specifically, fly ashes with R-factors <0, CaO/SiO_2 ratios <10%, and $CaO/(Al_2O_3+SiO_2)$ ratios <6% tend to exhibit better sulfate resistance. These values may serve as guidance for mixture design and for selecting suitable fly ashes in cementitious systems exposed to sulfate environments.

5. Conclusions

This study develops a meso-scale numerical framework to investigate the degradation mechanisms of low-calcium fly ash–blended cementitious paste and mortar systems under external sulfate attack (ESA), assuming fully saturated and isothermal conditions after an initial curing stage. The model integrates chemical reactions, ion transport, calcium leaching, porosity evolution, and mechanical damage to model the deterioration process. To capture the heterogeneous porosity distribution, a random porosity field is introduced. The framework systematically explores the coupled effects of sulfate

Table 10
Inputs and outputs of 30 modelled cases.

Fly ash	CA (mol/m^3)	CH (mol/m^3)	C-S-H (mol/m^3)	$\varnothing_a$ (%)	a_s (m^3/mol)	q	Expansion (%)
10% FA1	241.69	3238.9	2008.9	18.31	1.59E-04	2.25	0.21385
10% FA2	245.46	3274.8	2045.1	17.99	1.60E-04	2.24	0.2663
10% FA3	237.77	3190.5	1977	18.56	1.59E-04	2.26	0.16491
10% FA4	239.69	3202.6	1994.6	18.48	1.59E-04	2.26	0.18533
10% FA5	245.16	3261.9	2048.5	17.95	1.60E-04	2.24	0.26755
10% FA6	241.5	3210.7	2013	18.38	1.59E-04	2.26	0.20603
10% FA7	238.94	3202.4	1992.6	18.39	1.59E-04	2.26	0.1878
10% FA8	243.77	3259.2	2033.3	18.04	1.60E-04	2.25	0.25092
10% FA9	238.53	3222.3	1990.3	18.23	1.59E-04	2.26	0.19892
10% FA10	245.24	3271.1	2047.5	17.92	1.60E-04	2.24	0.27033
20% FA1	229.32	2951.2	1959.9	18.37	1.62E-04	2.19	0.14528
20% FA2	233.48	2966.7	1999.2	18.01	1.63E-04	2.18	0.20653
20% FA3	224.68	2909	1927.8	18.62	1.62E-04	2.2	0.091513
20% FA4	227.08	2909.4	1949.3	18.56	1.62E-04	2.2	0.11444
20% FA5	232.96	2940.6	2006	17.94	1.63E-04	2.18	0.20842
20% FA6	229.28	2902.2	1972.3	18.48	1.62E-04	2.19	0.13494
20% FA7	225.8	2908.5	1944.9	18.38	1.62E-04	2.19	0.12081
20% FA8	231.36	2953.6	1986.3	18.03	1.63E-04	2.18	0.19248
20% FA9	224.87	2939.3	1935	18.11	1.62E-04	2.19	0.13789
20% FA10	232.99	2956.1	2002.4	17.90	1.63E-04	2.18	0.21182
30% FA1	222.36	2657.4	1907.2	18.47	1.66E-04	2.12	0.10677
30% FA2	227.08	2652.3	1949.7	18.06	1.66E-04	2.1	0.17447
30% FA3	216.97	2621.4	1875	18.7	1.65E-04	2.13	0.018989
30% FA4	219.8	2610.1	1900.3	18.67	1.65E-04	2.12	0.058623
30% FA5	226.45	2613	1959.8	17.96	1.66E-04	2.1	0.1759
30% FA6	222.38	2587.4	1928	18.61	1.66E-04	2.12	0.092264
30% FA7	218.22	2608.4	1893.5	18.41	1.65E-04	2.12	0.072558
30% FA8	224.62	2641.7	1935.6	18.04	1.66E-04	2.11	0.15746
30% FA9	217.2	2650.2	1876.1	18.02	1.65E-04	2.12	0.10398
30% FA10	226.48	2634.8	1953.5	17.90	1.66E-04	2.1	0.18129

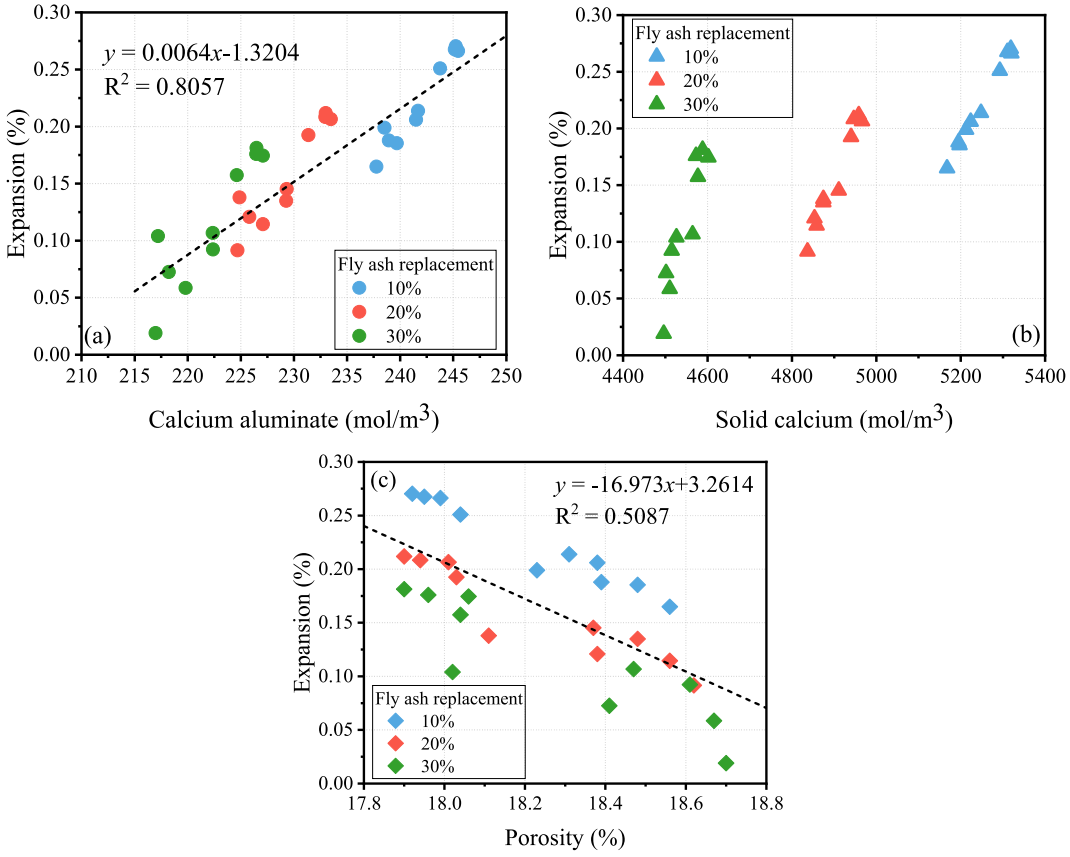


Fig. 16. Modelled expansion strain field submerged in 5% Na_2SO_4 solution after 1000 days (a) Effect of CA (b) Effect of solid calcium content (c) Effect of initial porosity.

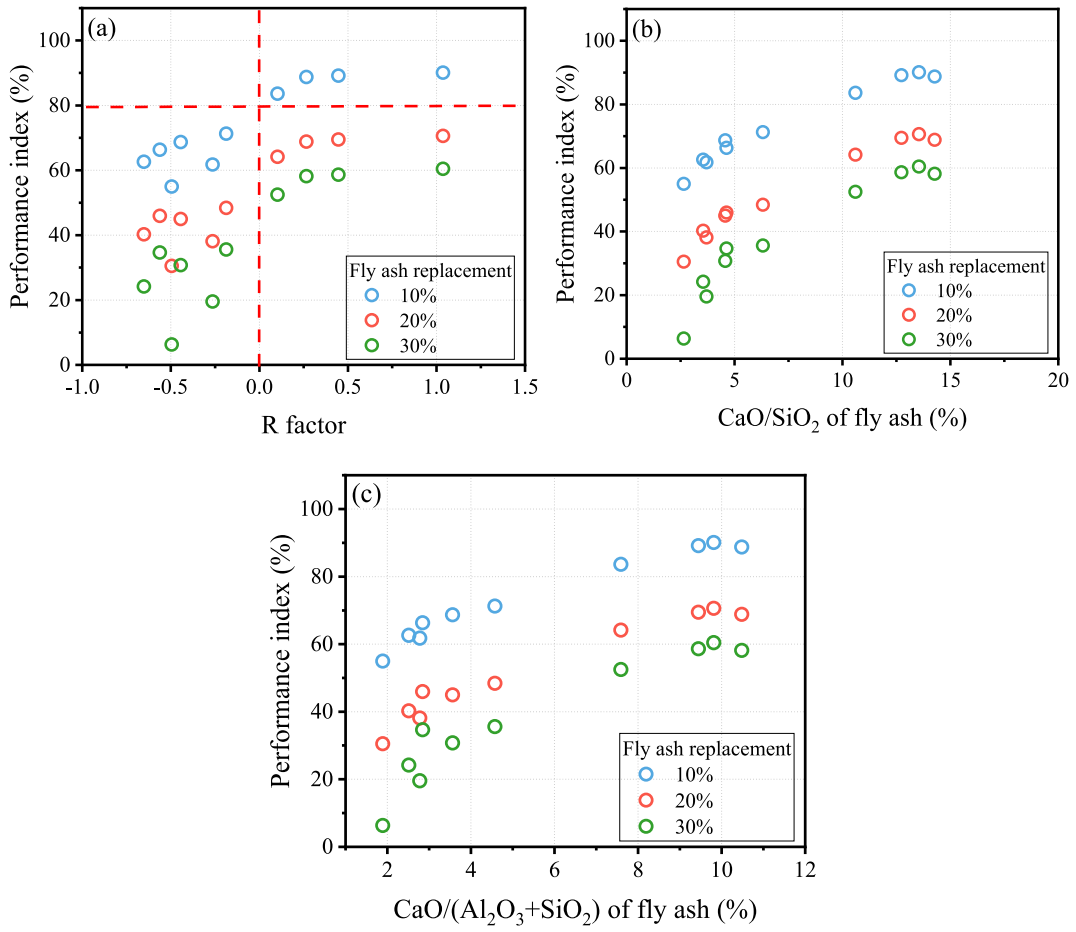


Fig. 17. Relationship between fly ash indicators and ESA performance (a) R-factor (b) CaO/SiO_2 (c) Ca/(Al + Si).

attack and calcium leaching, the influence of initial material properties modified by fly ash incorporation, and the impact of initial mineral compositions on expansion strain distribution. In summary, the key contributions and findings are as follows.

1) The proposed model accurately predicts the expansion behavior of fly ash–blended specimens with varying fly ash content, based on a coupled analysis of hydration and pozzolanic reactions. Results demonstrate that low-calcium fly ash reduces expansion strain by lowering the contents of CH and CA and decreasing initial porosity. At the early stage of sulfate exposure, expansion develops gradually as expansive products form and fill the pore space. With continued exposure, expansion accelerates due to product accumulation. Additionally, smaller specimens exhibit greater expansion, and higher sulfate concentrations result in both increased expansion and a deeper penetration of sulfate ions.
2) Interaction between sulfate attack and calcium leaching should be fully considered. Ignoring calcium leaching results in significantly lower expansion compared to the proposed model, which accounts for all influencing factors. This is due to the lower concentration of calcium ions available for reaction. Additionally, sulfate ions can accelerate the calcium leaching process, and neglecting this sulfate-induced acceleration leads to an underestimation of the predicted expansion. It can be concluded that the interaction between calcium leaching and sulfate attack has a significant impact on chemical reactions and should be thoroughly considered in numerical modeling of ESA.
3) By incorporating fly ashes with varying mineralogical compositions at replacement levels of 10–30%, the modelled results reveal that among the initial hydration products, CA content exerts the most significant influence on expansion behavior. While solid calcium content shows a positive correlation with ESA resistance, this trend is evident only under the same replacement level. Initial porosity is generally negatively correlated with ESA resistance, but exhibits high variability, limiting its reliability as a standalone indicator.
4) The relationships between fly ash-based indicators and ESA resistance were quantitatively evaluated. Although scatter will limit their predictive accuracy, lower indicator values combined with higher fly ash replacement levels are generally associated with improved sulfate resistance, particularly for fly ashes with R-factors <0, $CaO/SiO_2 < 10\%$, and $CaO/(Al_2O_3 + SiO_2) < 6\%$.

Despite the above findings, several limitations remain, which should be addressed in future research. First, factors such as unsaturated conditions, temperature fluctuations, and drying–wetting cycles should be incorporated to more accurately simulate the degradation process under realistic environmental conditions. Second, for fly ash–blended systems, the applicability of the three-stage calcium leaching model and the determination of the buffer coefficient require further investigation. Third, a more in-depth analysis of expansion mechanisms—particularly the volume increase theory and crystallization pressure theory—is needed to improve the understanding of sulfate-induced expansion. Finally, the current study focuses on mortar and paste; future work should extend to concrete to investigate the influence of aggregates and the interfacial transition zone (ITZ) on sulfate resistance.

CRediT authorship contribution statement

Qing-feng Liu: Writing – review & editing, Writing – original draft, Software, Resources, Project administration, Methodology, Investigation, Funding acquisition, Conceptualization. **Qing-xiang Xiong:**

Writing – review & editing, Visualization, Software, Investigation, Formal analysis. **Lie Ji:** Writing – original draft, Investigation, Formal analysis, Data curation. **Jun Yang:** Writing – review & editing, Validation, Resources, Data curation. **Jianting Zhou:** Writing – review & editing, Validation, Resources. **Zhaozheng Meng:** Visualization, Validation, Investigation, Data curation. **Yu Zhou:** Writing – review & editing, Validation, Formal analysis. **Liang-yu Tong:** Writing – review & editing, Validation, Resources, Methodology, Investigation, Funding acquisition, Conceptualization.

Declaration of competing interest

The authors declare that they have no known competing financial interests or personal relationships that could have appeared to influence the work reported in this paper.

Acknowledgements

This work was funded by the National Natural Science Foundation of China (52478264, 524B2119, W2421078), the Natural Science Foundation of Chongqing Municipality, China (cstb2024nscq-jqX0007), China Scholarship Council program (202306230277), and the State Key Laboratory of Mountain Bridge and Tunnel Engineering (SKLBT-ZD2201).

Data availability

The data that has been used is confidential.

References

[1] B. Dong, W. Ding, S. Qin, N. Han, G. Fang, Y. Liu, F. Xing, S. Hong, Chemical self-healing system with novel microcapsules for corrosion inhibition of rebar in concrete, Cement Concr. Compos. 85 (2018) 83–91.
[2] Y.-J. Tang, X.-B. Zuo, G.-J. Yin, H. Davoudi, X.-N. Li, Influence of calcium leaching on chloride diffusivity in cement-based materials, Constr. Build. Mater. 174 (2018) 310–319.
[3] R. El-Hachem, E. Rozière, F. Grondin, A. Loukili, Multi-criteria analysis of the mechanism of degradation of Portland cement based mortars exposed to external sulphate attack, Cement Concr. Res. 42 (10) (2012) 1327–1335.
[4] P. Gao, X. Gao, L.-y. Tong, et al., Multi-physics coupling model of chloride-induced rebar corrosion and concrete cracking in reinforced concrete structure, Comput. Struct. 326 (2026) 108231.
[5] C-l Zhang, W-k Chen, S. Mu, B. Šavija, Q-f Liu, Numerical investigation of external sulfate attack and its effect on chloride binding and diffusion in concrete, Constr. Build. Mater. 285 (2021) 122806–122817.
[6] K. Wang, J. Guo, L. Yang, Effect of dry–wet ratio on sulfate transport-reaction mechanism in concrete, Constr. Build. Mater. 302 (2021) 124418.
[7] K. Sotiriadis, E. Nikolopoulou, S. Tsivilis, Sulfate resistance of limestone cement concrete exposed to combined chloride and sulfate environment at low temperature, Cement Concr. Compos. 34 (8) (2012) 903–910.
[8] R. Tixier, Microstructural Development and Sulfate Attack Modeling in Blended Cement-based Materials, Arizona State University, 2000.
[9] R. Ragoug, O.O. Metalssi, F. Barberon, J.-M. Torrenti, N. Roussel, L. Divet, J.-B. d'Espinose de Lacaillerie, Durability of cement pastes exposed to external sulfate attack and leaching: physical and chemical aspects, Cement Concr. Res. 116 (2019) 134–145.
[10] M.S. Hasan, S. Setunge, D.W. Law, T.C.K. Molyneaux, Predicting life expectancy of concrete septic tanks exposed to sulfuric acid attack, Mag. Concr. Res. 65 (13) (2013) 793–801.
[11] T. Ikumi, I. Segura, Numerical assessment of external sulfate attack in concrete structures. A review, Cement Concr. Res. 121 (2019) 91–105.
[12] W. Müllauer, R.E. Beddoe, D. Heinz, Effect of carbonation, chloride and external sulphates on the leaching behaviour of major and trace elements from concrete, Cement Concr. Compos. 34 (5) (2012) 618–626.
[13] N. Cefis, C. Comi, Chemo-mechanical modelling of the external sulfate attack in concrete, Cement Concr. Res. 93 (2017) 57–70.
[14] T. Ikumi, S.H.P. Cavalaro, I. Segura, A. Aguado, Alternative methodology to consider damage and expansions in external sulfate attack modeling, Cement Concr. Res. 63 (2014) 105–116.
[15] E. Sakai, S. Miyahara, S. Ohsawa, S.-H. Lee, M. Daimon, Hydration of fly ash cement, Cement Concr. Res. 35 (6) (2005) 1135–1140.
[16] V.G. Papadakis, Effect of fly ash on Portland cement systems: part I. Low-calcium fly ash, Cement Concr. Res. 29 (11) (1999) 1727–1736.
[17] C. Yu, W. Sun, K. Scrivener, Mechanism of expansion of mortars immersed in sodium sulfate solutions, Cement Concr. Res. 43 (2013) 105–111.
[18] E. Samson, J. Marchand, Modeling the transport of ions in unsaturated cement-based materials, Comput. Struct. 85 (23) (2007) 1740–1756.
[19] E. Rozière, A. Loukili, R. El Hachem, F. Grondin, Durability of concrete exposed to leaching and external sulphate attacks, Cement Concr. Res. 39 (12) (2009) 1188–1198.
[20] H. Bao, M. Yu, L. Xu, M. Saafi, J. Ye, Experimental study and multi-physics modelling of concrete under supercritical carbonation, Constr. Build. Mater. 227 (2019) 116680.
[21] K. Liu, D. Sun, A. Wang, G. Zhang, J. Tang, Long-term performance of blended cement paste containing fly ash against sodium sulfate attack, J. Mater. Civ. Eng. 30 (12) (2018) 04018309.
[22] Z. Meng, Q-f Liu, N. Ukrainczyk, S. Mu, Y. Zhang, G. De Schutter, Numerical study on the chemical and electrochemical coupling mechanisms for concrete under combined chloride-sulfate attack, Cement Concr. Res. 175 (2024) 107368.
[23] K. Ramyar, G. İnan, Sodium sulfate attack on plain and blended cements, Build. Environ. 42 (3) (2007) 1368–1372.
[24] M. Sumer, Compressive strength and sulfate resistance properties of concretes containing class F and class C fly ashes, Constr. Build. Mater. 34 (2012) 531–536.
[25] H.N. Atahan, D. Dikme, Use of mineral admixtures for enhanced resistance against sulfate attack, Constr. Build. Mater. 25 (8) (2011) 3450–3457.
[26] N. Ghafoori, M. Najimi, H. Diawara, M.S. Islam, Effects of class F fly ash on sulfate resistance of type V Portland cement concretes under continuous and interrupted sulfate exposures, Constr. Build. Mater. 78 (2015) 85–91.
[27] J. Liu, Y. Wang, Predicting the chloride diffusion in concrete incorporating fly ash by a multi-scale model, J. Clean. Prod. 330 (2022) 129767.
[28] B. Park, Y.C. Choi, Hydration and pore-structure characteristics of high-volume fly ash cement pastes, Constr. Build. Mater. 278 (2021).
[29] H. Zhao, X. Qin, J. Liu, L. Zhou, Q. Tian, P. Wang, Pore structure characterization of early-age cement pastes blended with high-volume fly ash, Constr. Build. Mater. 189 (2018) 934–946.
[30] Q. Zeng, K. Li, T. Fen-chong, P. Dangla, Pore structure characterization of cement pastes blended with high-volume fly-ash, Cement Concr. Res. 42 (1) (2012) 194–204.
[31] M.M.A. Elahi, C.R. Shearer, A. Naser Rashid Reza, A.K. Saha, M.N.N. Khan, M. M. Hossain, P.K. Sarker, Improving the sulfate attack resistance of concrete by using supplementary cementitious materials (SCMs): a review, Constr. Build. Mater. 281 (2021) 122628.
[32] M. Ashraf, M.F. Iqbal, M. Rauf, M.U. Ashraf, A. Ulhaq, H. Muhammad, Q-f Liu, Developing a sustainable concrete incorporating bentonite clay and silica fume: mechanical and durability performance, J. Clean. Prod. 337 (2022) 130315.
[33] K. Chen, Z. He, J. Liu, Y. Lin, L. Jia, Long-term morphological evolution and its mechanism of lingdingyang Estuary: interferences from anthropogenic forcings, Mar. Geol. 450 (2022) 106856.
[34] Z. Meng, Q-f Liu, J. Xia, Y. Cai, X. Zhu, Y. Zhou, L. Pel, Mechanical–transport–chemical modeling of electrochemical repair methods for corrosion-induced cracking in marine concrete, Comput. Aided Civ. Infrastruct. Eng. 37 (14) (2022) 1854–1874.
[35] Q. Liu, Z. Meng, A review of numerical modelling for predicting concrete durability degradation under multiple deterioration mechanisms, J. Chin. Ceram. Soc. 54 (02) (2026) 811–820.
[36] S. Sarkar, S. Mahadevan, J.C.L. Meeussen, H. van der Sloot, D.S. Kosson, Numerical simulation of cementitious materials degradation under external sulfate attack, Cement Concr. Compos. 32 (3) (2010) 241–252.
[37] Y. Yu, Y.X. Zhang, A. Khennane, Numerical modelling of degradation of cement-based materials under leaching and external sulfate attack, Comput. Struct. 158 (2015) 1–14.
[38] M. Zhang, S. Qin, H. Lyu, C. Chen, D. Zou, A. Zhou, Y. Li, T. Liu, A transport-chemical-physical–mechanical model for concrete subjected to external sulfate attack and drying–wetting cycles, Eng. Fract. Mech. 293 (2023) 109726.
[39] S. Qin, D. Zou, T. Liu, A. Jivkov, A chemo-transport-damage model for concrete under external sulfate attack, Cement Concr. Res. 132 (2020) 106048.
[40] K. Haga, S. Sutou, M. Hironaga, S. Tanaka, S. Nagasaki, Effects of porosity on leaching of Ca from hardened ordinary Portland cement paste, Cement Concr. Res. 35 (9) (2005) 1764–1775.
[41] C. Neumann, E.F. Faria, dos Santos Acp, Concrete leaching of a hydroelectric powerhouse due to 40 years of exposure to river water, Constr. Build. Mater. 302 (2021) 124253.
[42] Q-f Liu, D. Easterbrook, J. Yang, L-y Li, A three-phase, multi-component ionic transport model for simulation of chloride penetration in concrete, Eng. Struct. 86 (2015) 122–133.
[43] Q-f Liu, G-l Feng, J. Xia, J. Yang, L-y Li, Ionic transport features in concrete composites containing various shaped aggregates: a numerical study, Compos. Struct. 183 (2018) 371–380.
[44] Q. Nie, C. Zhou, H. Li, X. Shu, H. Gong, B. Huang, Numerical simulation of fly ash concrete under sulfate attack, Constr. Build. Mater. 84 (2015) 261–268.
[45] K. Nakarai, T. Ishida, K. Maekawa, Modeling of calcium leaching from cement hydrates coupled with micro-pore formation, J. Adv. Concr. Technol. 4 (3) (2006) 395–407.
[46] D. Planel, J. Sercombe, P. Le Bescop, F. Adenot, J.M. Torrenti, Long-term performance of cement paste during combined calcium leaching–sulfate attack: kinetics and size effect, Cement Concr. Res. 36 (1) (2006) 137–143.
[47] X. Liu, P. Feng, X. Yu, J. Huang, Decalcification of calcium silicate hydrate (C-S-H) under aggressive solution attack, Constr. Build. Mater. 342 (2022) 127988.
[48] E. Samson, J. Marchand, K.A. Snyder, Calculation of ionic diffusion coefficients on the basis of migration test results, Mater. Struct. 36 (2003) 156–165.

[49] D. Zou, M. Zhang, S. Qin, T. Liu, W. Tong, A. Zhou, A. Jivkov, Calcium leaching from cement hydrates exposed to sodium sulfate solutions, Constr. Build. Mater. 351 (2022) 128975.
[50] Q.T. Phung, N. Maes, D. Jacques, J. Perko, G. De Schutter, G. Ye, Modelling the evolution of microstructure and transport properties of cement pastes under conditions of accelerated leaching, Constr. Build. Mater. 115 (2016) 179–192.
[51] B. Gérard, C. Le Bellego, O. Bernard, Simplified modelling of calcium leaching of concrete in various environments, Mater. Struct. 35 (2002) 632–640.
[52] S. Kamali, B. Gérard, M. Moranville, Modelling the leaching kinetics of cement-based materials—influence of materials and environment, Cement Concr. Compos. 25 (4-5) (2003) 451–458.
[53] Y. Wang, Q. Yuan, D. Deng, Modelling calcium leaching kinetics of cement asphalt paste, Mater. Struct. 51 (5) (2018) 133.
[54] K. Wan, Y. Li, W. Sun, Experimental and modelling research of the accelerated calcium leaching of cement paste in ammonium nitrate solution, Constr. Build. Mater. 40 (2013) 832–846.
[55] X. Gao, Q-f Liu, Y. Cai, L-y Tong, Z. Peng, Q.X. Xiong, G. De Schutter, A new model for investigating the formation of interfacial transition zone in cement-based materials, Cement Concr. Res. 187 (2025) 107675.
[56] L-y Tong, Q-f Liu, E. Gruyaert, N.M. Alderete, Q-x Xiong, N. De Belie, Experimental and numerical study on carbonation of blast-furnace slag concrete considering the microstructural evolution, Cement Concr. Res. 200 (2026) 108084.
[57] Z. Wang, L. Tong, Q. Xiong, et al., Numerical study of chloride diffusion in unsaturated cementitious materials based on pore network, J. Build. Mater. 29(1) (2026) 39-48+66.
[58] B. Ran, O. Omikrine-Metalssi, T. Fen-Chong, P. Dangla, K. Li, Impact of leaching and chlorides on sulfate attack for cement paste, Constr. Build. Mater. 376 (2023) 130881, 11.
[59] J-k Chen, M-q Jiang, J. Zhu, Damage evolution in cement mortar due to erosion of sulphate, Corros. Sci. 50 (9) (2008) 2478–2483.
[60] R. Tixier, B. Mobasher, Modeling of damage in cement-based materials subjected to external sulfate attack. I: formulation, J. Mater. Civ. Eng. 15 (4) (2003) 305–313.
[61] G.-J. Yin, X.-D. Wen, L. Miao, D. Cui, X.-B. Zuo, Y.-J. Tang, A review on the transport-chemo-mechanical behavior in concrete under external sulfate attack, Coatings 13 (1) (2023) 174.
[62] X. Gao, Z. Peng, L-y Tong, Y. Cai, J. Xiao, X. Geng, Q-f Liu, Effect of global aggregate distribution on interfacial transition zones in cement-based materials: an analytical-numerical study, Constr. Build. Mater. 458 (2025) 138278.
[63] Q. Xiong, Q. Liu, Salt crystallization-induced pore structure evolution and transport properties degradation in cementitious materials, J. Chin. Ceram. Soc. 54 (02) (2026) 470–483.
[64] L.Y. Tong, Q.F. Liu, X. Xu, Q.X. Xiong, D.C.W. Tsang, Effect of carbonation on transport properties of cementitious materials under different environmental conditions: A pore-scale modelling, J. Clean. Prod. 490 (2025) 144669.
[65] L-y Tong, Q-f Liu, Q. Xiong, Z. Meng, O. Amiri, M. Zhang, Modeling the chloride transport in concrete from microstructure generation to chloride diffusivity prediction, Comput. Aided Civ. Infrastruct. Eng. 40 (9) (2025) 1129–1149.
[66] L-y Tong, B. Šavija, M. Zhang, Q.X. Xiong, Q-f Liu, Chloride penetration in concrete under varying humidity and temperature changes: a numerical study, Constr. Build. Mater. 458 (2025) 138380.
[67] L. Lin, J. Chen, X. Zhang, X. Li, A novel 2-D random void model and its application in ultrasonically determined void content for composite materials, NDT E Int. 44 (3) (2011) 254–260.
[68] X.-Y. Wang, H.-S. Lee, A model for predicting the carbonation depth of concrete containing low-calcium fly ash, Constr. Build. Mater. 23 (2) (2009) 725–733.
[69] J.J. Thomas, J.J. Biernacki, J.W. Bullard, S. Bishnoi, J.S. Dolado, G.W. Scherer, A. Luttge, Modeling and simulation of cement hydration kinetics and microstructure development, Cement Concr. Res. 41 (12) (2011) 1257–1278.
[70] L. D'Aloia, G. Chanvillard, Determining the "apparent" activation energy of concrete: Ea—numerical simulations of the heat of hydration of cement, Cement Concr. Res. 32 (8) (2002) 1277–1289.
[71] J. Atallah, F. Bignonnet, H. Ranaivomanana, S. Bonnet, An analytical model for the long term slag hydration kinetics in slag blended cement established from a large experimental database, Constr. Build. Mater. 448 (2024) 138160.
[72] K. Kinomura, T. Ishida, Enhanced hydration model of fly ash in blended cement and application of extensive modeling for continuous hydration to pozzolanic micro-pore structures, Cement Concr. Compos. 114 (2020) 103733.
[73] F. Xiang-peng, G. Li-ping, L. Jia-tao, S. Hao-ran, C. Hai-tao, R. Zi-qing, Modeling and analysis of hydration in cementitious composites with ultra-high dosage of fly ash: hydrates and microstructure evolutions, Constr. Build. Mater. 470 (2025) 140557.
[74] M. Yu, H. Bao, J. Ye, Y. Chi, The effect of random porosity field on supercritical carbonation of cement-based materials, Constr. Build. Mater. 146 (2017) 144–155.
[75] Z. Jiang, Y. Pan, C. Fu, W. Li, Y. Wang, W.-J. Long, Three-dimensional pore structure characterization of cement paste by X-ray computed tomography (XCT) and focused ion beam/scanning electron microscopy (FIB/SEM), Constr. Build. Mater. 383 (2023) 131379.
[76] J.M. Khatib, P.S. Mangat, Porosity of cement paste cured at 45 °C as a function of location relative to casting position, Cement Concr. Compos. 25 (1) (2003) 97–108.
[77] M.L. Nehdi, A.R. Suleiman, A.M. Soliman, Investigation of concrete exposed to dual sulfate attack, Cement Concr. Res. 64 (2014) 42–53.
[78] A.E. Idiart, C.M. López, I. Carol, Chemo-mechanical analysis of concrete cracking and degradation due to external sulfate attack: a meso-scale model, Cement Concr. Compos. 33 (3) (2011) 411–423.
[79] D. Somette, Critical transport and failure in continuum crack percolation, J. Phys. 49 (8) (1988) 1365–1377.
[80] L-y Tong, Q.X. Xiong, Z. Zhang, X. Chen, G. Ye, Q-f Liu, A novel lattice model to predict chloride diffusion coefficient of unsaturated cementitious materials based on multi-typed pore structure characteristics, Cement Concr. Res. 176 (2024) 107351.
[81] Q.X. Xiong, F. Meftah, Determination on pore size distribution by a probabilistic porous network subjected to salt precipitation and dissolution, Comput. Mater. Sci. 195 (2021) 110491.
[82] Z. Liu, X. Li, D. Deng, G. De Schutter, L. Hou, The role of Ca(OH)2 in sulfate salt weathering of ordinary concrete, Constr. Build. Mater. 123 (2016) 127–134.
[83] M.F. Najjar, M.L. Nehdi, A.M. Soliman, T.M. Azabi, Damage mechanisms of two-stage concrete exposed to chemical and physical sulfate attack, Constr. Build. Mater. 137 (2017) 141–152.
[84] R.J. Flatt, G.W. Scherer, Thermodynamics of crystallization stresses in DEF, Cement Concr. Res. 38 (3) (2008) 325–336.
[85] G.W. Scherer, Stress from crystallization of salt, Cement Concr. Res. 34 (9) (2004) 1613–1624.
[86] B. Bary, N. Leterrier, E. Deville, P. Le Bescop, Coupled chemo-transport-mechanical modelling and numerical simulation of external sulfate attack in mortar, Cement Concr. Compos. 49 (2014) 70–83.
[87] Q-f Liu, Z. Hu, X-e Wang, H. Zhao, K. Qian, L-j Li, Z. Meng, Numerical study on cracking and its effect on chloride transport in concrete subjected to external load, Constr. Build. Mater. 325 (2022) 126797.
[88] E. Charlaix, Percolation threshold of a random array of discs: a numerical simulation, J. Phys. Math. Gen. 19 (9) (1986) L533.
[89] E. Samson, G. Lemaire, J. Marchand, J.J. Beaudoin, Modeling chemical activity effects in strong ionic solutions, Comput. Mater. Sci. 15 (3) (1999) 285–294.
[90] D. Sun, K. Wu, H. Shi, L. Zhang, L. Zhang, Effect of interfacial transition zone on the transport of sulfate ions in concrete, Constr. Build. Mater. 192 (2018) 28–37.
[91] L-x Mao, L-y Li, Y. Wang, Q-f Liu, Physicochemical modelling in chlorides migration in concrete with account of multi-species coupling, reaction kinetic and pore evolution, Constr. Build. Mater. 460 (2025) 139707.
[92] L-y Tong, Q.X. Xiong, M. Zhang, Z. Meng, F. Meftah, Q-f Liu, Multi-scale modelling and statistical analysis of heterogeneous characteristics effect on chloride transport properties in concrete, Constr. Build. Mater. 367 (2023) 130096.
[93] Z. Peng, Q-x Xiong, X. Zhou, X. Gao, X.-Y. Zhao, Z. Meng, Q-f Liu, A porosity-based mechanics model for studying crack evolution from ITZ to mortar matrix in concrete, Comput. Methods Appl. Mech. Eng. 444 (2025) 118085.
[94] Q-f Liu, Y. Cai, H. Peng, Z. Meng, S. Mundra, A. Castel, A numerical study on chloride transport in alkali-activated fly ash/slag concretes, Cement Concr. Res. 166 (2023) 107094.
[95] A. Mardani-Aghabaglou, G. İnan Sezer, K. Ramyar, Comparison of fly ash, silica fume and metakaolin from mechanical properties and durability performance of mortar mixtures view point, Constr. Build. Mater. 70 (2014) 17–25.
[96] O.S. Baghabra, M. Maslehuddin, M.M. Saadi, Effect of magnesium sulfate and sodium sulfate on the durability performance of plain and blended cements, Mater. J. 92 (1) (1995) 15–24.
[97] Z. Zhang, X. Jin, W. Luo, Long-term behaviors of concrete under low-concentration sulfate attack subjected to natural variation of environmental climate conditions, Cement Concr. Res. 116 (2019) 217–230.
[98] M.D. Cohen, A. Bentur, Durability of portland cement-silica fume pastes in magnesium and sodium sulfate solutions, Mater. J. 85 (3) (1988) 148–157.